TÉCNICO LISBOA

Characterization of methane inverse diffusion flames in a multi-slot burner

Miguel Filipe Neves Ribeiro

Thesis to obtain the Master of Science Degree in

Mechanical Engineering

Supervisors: Prof. Edgar Caetano Fernandes
Eng. Filipe João Marques Quintino

Examination Committee

Chairperson: Prof. Carlos Frederico Neves Bettencourt da Silva
Supervisor: Prof. Edgar Caetano Fernandes
Member of the Committee: Prof. Teodoro José Pereira Trindade

June 2019

Dedicated to someone special...

Acknowledgments

A entrega desta tese simboliza o término de uma importante viagem de aprendizagem e formação. A chegada a este ponto não teria sido possível sem o apoio de muitas pessoas que de uma maneira ou de outra deixaram o seu cunho ao longo destes anos.

Gostaria primeiramente de deixar uma palavra de agradecimento e apreço ao Professor Edgar Fernandes, não só pelo apoio e motivação prestados ao longo da elaboração desta tese, mas também devido ao entusiasmo transmitido no leccionamento de diversas cadeiras no técnico, momentos em que, na verdade, decidi abordar esta área de investigação.

Deixo também um especial agradecimento ao Filipe Quintino pelo imenso apoio e disponibilidade a todos os momentos ao longo da elaboração desta tese.

A todos os meus colegas de laboratório e em especial ao João Xavier, Rui Araújo e André Korolev incansáveis no companheirismo e entreajuda em todos os momentos desta jornada. São amizades que ficam e hão sempre de perdurar.

Ao João Pires pelo importante auxílio prestado no inicio do desenvolvimento deste trabalho, e aos restantes membros do IN+ um sincero obrigado.

Por fim à Renata Rodrigues pela infinita paciência e apoio. E a toda a minha familia a quem dedico esta tese.

Resumo

As Chamas de Difusão Inversa (IDF) apresentam várias características potencialmente vantajosas para o objetivo de controlar as emissões nocivas e alcançar maior eficiência. Combinando benefícios de uma chama de pré-mistura e difusão, a IDF demonstra uma maior abrangência e estabilidade na queima de misturas pobres e uma menor produção de NO_x e fuligem do que uma chama de difusão normal, evitando simultaneamente o *flashback*.

Foi estabelecida uma gama completa de chamas de metano utilizando um queimador de ranhuras, partindo de um regime de difusão pura até uma razão de equivalência global de 0,2. Utilizou-se espectroscopia de quimiluminescência para medir os valores locais de ϕ (razão de equivalência) e PIV para obter os mapas vetoriais de velocidade de cada tipo de chama. Foram realizadas várias medições de velocidade a diferentes alturas de chama e equivalentes escoamentos isotérmicos, permitindo uma comparação entre os casos isotérmico e de chama e o estudo da evolução do perfil de velocidade da chama.

Para a gama de IDF estabelecida foram identificados quatro diferentes tipos de chama, dos quais três, Tipo II, III e IV foram estudados mais aprofundadamente com as técnicas mencionadas anteriormente. Verificaram-se transformações morfológicas acentuadas, desde um duplo regime aproximado a uma pré-mistura parcial com produção de fuligem, até uma chama azul de topo aberto com intensa mistura a montante. A razão entre velocidades de ar e combustível, V_r, demonstrou-se como um parâmetro importante na definição das morfologias de chama, devido ao seu papel fulcral na mistura ar-combustível. Constatou-se que a estrutura de pescoço, característica da chama tipo IV inicia a sua formação a $Re_{ar} = 355$, funcionando como um mecanismo de estabilização estrutural, apresentando uma zona de recirculação devido à alta pressão em torno do ponto de estagnação de impacto.

Palavras-chave: Chama de difusão inversa, espectroscopia, velocimetria por imagem de particulas, queimador de ranhuras, morfologia, quimiluminescência

Abstract

Inverse diffusion flames (IDF), present several potentially advantageous characteristics towards the goal of controlling noxious emissions and achieving a higher efficiency. Combining benefits of a premixed and diffusion flame, IDF have shown an extended lean flammability range and a smaller production of NO_x and soot than a normal diffusion flame while simultaneously avoiding flashback.

A complete methane IDF range in a multi-slot burner was established, from pure diffusion regime to a global equivalence ratio of 0.2. Chemiluminescence spectroscopy was utilized to measure local ϕ values and PIV was applied to obtain the velocity vector maps of each flame type, a number of velocity measurements were made at different flame heights and at their flowrate-equivalent isothermal cases. Permitting a comparison between the isothermal and flame cases and the study of the flame velocity profile evolution.

For the established IDF flame range four different flame types were identified, of which three, Type II, III and IV were studied more in depth with the previously mentioned techniques. Accentuated morphology transformations were verified, from a dual-regime, resembling a soot producing partial premixed flame to a totally blue open top flame with intense upstream mixing. The air-fuel velocity ratio (V_r) was found to be an important governing parameter in the definition of the flame structures, due to its role in the air-fuel jet mixing. The neck structure characteristic of flame type IV was formed at $Re_{air} = 355$, functioning as a structural stabilization mechanism, presenting a recirculation zone due to the high pressure around the impingement stagnation point.

Keywords: Inverse diffusion flame, chemiluminescence, spectroscopy, particle image velocimetry, slot burner, morphology

Contents

List of Tables

List of Figures

Nomenclature

Greek symbols

κ	Thermal conductivity coefficient.
μ	Molecular viscosity coefficient.
ϕ	Equivalence ratio.
ρ	Density.

Roman symbols

p	Pressure.
$\mathbf{u}$	Velocity vector.
u, v, w	Velocity Cartesian components.

Subscripts

max	Maximum.
x, y, z	Cartesian components.
air	Respective to the air jet.
fuel	Respective to the fuel jet.
g	Global parameter.
iso	Isothermal condition.
r	Ratio.
ref	Reference condition.
st	Stoichiometric conditions.

Superscripts

*	Radical denomination
T	Transpose.

Chemical Species

C_2	Dicarbon.
CH_4	Methane.
CH	Methylidyne radical.
CO_2	Carbon dioxide.
CO	Carbon monoxide.
H_2O	Water.
H_2	Hydrogen (molecule).
N_2	Nitrogen (molecule).
O_2	Oxygen (molecule).
OH	Hydroxyl radical.

Acronyms

1D	One-Dimensional
2D	Two-Dimensional
3D	Three-Dimensional
CAP	Circumferential Arranged Ports burner
CCD	Charged Coupled Device
CoA	Coaxial burner
IA	Interrogation Area
IDF	Inverse Diffusion Flame
NDF	Normal Diffusion Flame
OI	Oxygen Index
PIV	Particle Image Velocimetry
PLIF	Planar Laser Induced Fluorescence

Chapter 1

Introduction

1.1 Motivation

Since its inception, mankind has demonstrated incredible ambition and resolve towards progress, developing numerous tools with this objective in sight. Overarching this journey is the need for energy. Combustion has proven from the get-go, to be a very important and versatile source of energy for mankind, ranging from the most primitive applications at the early stages of development to the widespread presence in industry, transportation, domestic applications and electrical energy production of today.

The combustion processes themselves have been the target of constant research and improvement, striving for a more complete understanding of the underlying mechanisms and the discovery of novel ways to optimize, apply and enhance these processes.

As societies evolved, their priorities were naturally ever-changing, at the turn of the century combustion saw tremendous advancements, from engines including the first plans for gas turbines, to the development of coal power plants. We had the future on our sights and the pace was tremendous, our dependency on these kinds of technology was well underway.

Although we were granted with a greatly improved quality of living, given to us not only by electricity generated with combustion but also its various other applications. This was not to be without a drawback, and so the environmental issues were ushered on, the damage demanded a rapid focus towards the development of new and improved technologies and applications of combustion that have the reduction and control of the emission of pollutants, combined with achieving higher energetic efficiency, as the central goal.

Nowadays there is an ongoing research effort focused on controlling three of the more dangerous pollutants emitted in combustion, CO, CO_2 and NO_x. This pushed developments towards leaner and colder flames, approaching the problem of flame stabilization within the parameters most ideal to minimize the emission of these noxious components. Inverse diffusion flames were initially investigated due to their potential in presenting several advantageous characteristics to achieve this desired behavior, a combination of a premixed flame and a diffusion flame that can have a larger flammability range than a premixed flame while also potentially producing less NO_x and soot than a normal diffusion flame (NDF).

This type of flames has great interest for application in industrial and domestic heating processes, therefore further research on this topic is valuable.

Another important factor in achieving the desired control of pollutants as well as the performance and efficiency, is the fuel choice. Numerous fuels have been utilized in combustion and in particular IDF (Inverse diffusion flames), ranging from LPG (liquid petroleum gas) to methane, ethylene and hydrogen. The latter is especially relevant nowadays, not only due to its unique thermo-physical properties but also due to the increasing renewable energy production sources and their inherent intermittent nature. In this context, the production of hydrogen can be seen as an opportunity to tackle one of the main issues of the energy field of the modern society, storage. The excess electricity produced by renewable sources such as wind, wave and solar energy, during their high output timeframes, can be utilized to produce hydrogen through hydrolysis and thermolysis, inciting a cyclic energy management approach [1].

1.2 State of the art

The vast majority of research and literature on diffusion flames has been devoted to normal flame configurations, where there is an environment of excess air surrounding the burning fuel. However, the research efforts into the inverse configuration have recently increased. The first mentions of inverse diffusion flames (IDF) in the literature happened at the beginning of the 20th century, with a brief mention by Friend in 1922 [2] and later with the height measurement of CO in IDF by Burke and Schumann in 1928 [3], pointing to a good agreement with predictions but without further details. The first substantial investigative efforts came with the work of Arthur and Napier in 1955 [4], focusing on the analysis of radiant emission comparison between the normal and inverse diffusion flames, demonstrating a striking difference in the much stronger luminosity and soot formation by the normal flame. In 1958, Weller presented axial temperature measurements and their comparison with normal diffusion flames (NDF) as part of a study on smoke and soot production in stoves.

After a considerable absence of developments, one of the main studies regarding this configuration was presented in 1985 by Wu and Essenhigh [5], this was motivated by an interest in studying the characteristics of carbon formation. Therefore, a thorough investigation was performed in order to identify the structure of laminar methane IDFs stabilized in a simple coaxial burner, with an approach based on visual appearance and air-fuel velocities. Six different regimes were identified along with the predicted temperature and stable species profiles, pointing to a nearly indistinguishable mathematical similarity between IDF and NDF. From this defining study two similar flames were shown to be the most representative of IDF, accounting for more than 50% of the flame map. These flames presented a parabolic blue combustion zone, with a yellow zone starting about 1/3 of the way up, forming a tapered truncated annulus with an open top and a shorter visual flame height in comparison with NDF.

Further developments into the study of soot formation were undertaken by Makel and Kennedy (1994) [6] and Du and Axelbaum (1995) [7], maintaining the use of a coaxial burner. Measurements of soot volume fraction and temperature were compared to the numerical predictions of a soot model previously applied to NDF, showing good agreement in the calculation of flame heights and soot residence times.

At this stage a third characterizing parameter for IDF (in addition to the previously mentioned air and fuel velocities) was starting to be widely used, the global equivalence ratio (ϕ_g). This quantity was directly adapted from the commonly utilized equivalence ratio (ϕ) for premixed flames, defined as the ratio between the fuel-to-oxidizer ratio and the stoichiometric fuel-to-oxidizer ratio. The use of this parameter in diffusion flames does not directly translate to a rich or lean mixture as in the premixed case, functioning only as an indicative reference measure of the air and fuel quantities that are being input into the burner separately.

Continuing the soot production mechanism studies, Shaddix et al. found the measurement of flame height revealed to be quite difficult due to the obscuring effect produced over the reaction zone associated with the IDF soot formation residing in a strongly radiating annular ring [8]. Due to this the measurement of the stoichiometric flame height using OH-Planar Laser-Induced Fluorescence (OH-PLIF) is particularly suited to IDF. This analysis was explored further by the works developed by Mikofski et al. during the early 2000s [9, 10]. These studies of laminar flames focused on the structure and height correlation of IDF with air flow variation, solidifying the description of a double structure, a partial premixed flame with a diffusion combustion regime downstream [9]. Regarding the luminous flame height (defined as the distance along the centerline from the burner exit to the point where flame luminosity is no longer visible to the naked eye), it was found to be greater than the reaction zone determined by OH-PLIF, due to the luminous soot present above the reaction zone [9]. As such, it is not an effective measurement of the flame height (defined as the distance from the burner exit to the point of stoichiometric fuel and oxidizer proportion along the flame centerline [11]), being the measurement to the maximum OH PLIF intensity on the flame centerline, a preferable approach.

All the previously mentioned studies utilized a co-annular (CoA) burners, with an interior air channel and a surrounding concentric annular air channel, as depicted in Figure 1.1(a). A second important burner configuration saw a comprehensive research effort to improve flame stability and mixing characteristics. The multi inverse diffusion flame, generated by a circumferential arranged ported burner (CAP) can be seen as a special case of traditional IDF, where the annular fuel jet is subdivided into multiple surrounding jets in a circumference centered on the singular central air jets as shown in Figure 1.1(b).

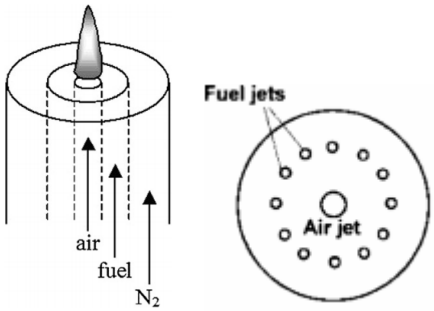

(a) CoA burner; (b) CAP burner; Source: [12]
Source: [10]

Figure 1.1: Main burner configurations

Sze et al showed that this arrangement provided intense fuel jet entrainment into the air jet, leading to better mixing and an improved flame stability at a lower Reynolds number [13–16]. This finding was

further corroborated by centerline oxygen measurements where a more intensive mixing was observed. The thermal characteristics of the multi-inverse diffusion flame were also subject to analysis, concluding that there is a general heat flux increase with the air Reynolds number and a maximum temperature zone located in the interface between the double structures (partial premix and diffusion combustion) [13].

Continuing the multi-inverse IDF approach, Zhen et al. [17] investigated the air nozzle length influence on the flame characteristics. A shorter nozzle produced a shorter potential core and an increase in both CO and CO_2 concentrations at the corresponding peak points. Additionally, the port diameter ratios were subject to optimization by Dong et al. finding a crucial effect on the behavior of the IDF by changing ar/fuel mixture dynamics (mixing and entrainment intensities), with a smaller air diameter a blue flame with better thermal characteristics and higher flame temperature as well as a wider operating range in terms of equivalence ratio. This approach was extended to the emission analysis, where a smaller air diameter resulted in more incomplete combustion, increasing CO and HC but decreasing NO_x, which is attributed to a lower volume of high temperature zone and shorter residence times [18].

Impingement heating was also seen as a potentially advantageous application for IDF, in particular for industrial environments, combining the advantages of a partially premixed flame (high flame temperature and soot-free flame structure) with the stability and safety characteristics of the diffusion flame (no flame flashback) [19]. This motivated the two part work developed by Dong et al. [20, 21], where the most favorable impingement flame morphology was found to be comprised of a short diffusion area and a large premixed flame torch separated by a neck contraction (a structure initially observed in the seminal study by Wu et al. [5]). Additionally it was also argued that the higher turbulence associated with the existence of the flame neck structure was responsible for the improvements in heat transfer.

In continuation of the heat transfer characterization, Zhen et al investigated the effect of swirling flow on IDF heat transfer rates to a flat surface. The swirl burners were utilized to increase the momentum exchange between air and fuel jets [22–24], resulting in an improvement in heat transfer rate and flame stability in comparison to the non-swirling counterparts [25]. The non-swirling IDF cool core created by the central air jet is eliminated by the swirl due to improved mixing, positioning the main combustion zone closer to the burner exit.

In regards to emission-focused studies, some researchers have found IDF capable of reaching extremely low levels of NO_x of under 18 ppm [26]. The peak NO_x production was found to occur close to stoichiometric conditions for CAP burners using liquefied petroleum gas (LPG), attaining a peak value at $\phi_g = 1.1$ [13, 27], this behaviour was delayed up to $\phi_g = 2.2$ for CoA burners [13]. The CO emission was found to decrease with the increase in ϕ_g [20].

Other research trends have been undertaken, in particular regarding the addition of different fuel components or oxidizers, Escudero et al. [28] examined the effect of the oxygen index (OI), which is defined as the molar concentration of oxygen in the oxidizer stream (composed by oxygen and nitrogen in the referred study), on the soot volume fraction and soot temperature, detecting an increase in soot volume fraction alongside the OI, attributing this behavior to the increase in temperature and soot formation.

The more recent investigative efforts on fuel additives focused on the effects of hydrogen addition in IDF, Miao et al. [12, 29] found that hydrogen enrichment up to 50% in LPG IDF with a CAP burner, can improve the stability (in particular reducing the lean blowout limit) and decrease the flame height for rich regimes, sustaining a lower global energy consumption.

Focusing now on the approaches more closely related to the present study, in particular the use of multi slot burners, two relevant studies have been undertaken utilizing this burner configuration, where the two concentric channels (oxidizer and surrounding fuel) are substituted by a central rectangular air slot with two adjacent parallel fuel slots. Shaddix et al. [8] focused on a comparative analysis between normal and inverse diffusion flames for this particular burner geometry at very specific flow rates, identifying the inversion in OH and policyclic aromatic hydrocarbons (PAH, these are formed in incomplete combustion and are associated with soot production) Laser-Induced-Fluorescence (LIF) layer positioning (shown in Figure 1.2(a)) for both methane and ethylene flames. Furthermore IDF were found relatively unstable in comparison to the NDF. Later with the work of Abdelal et al. [30] the focus was shifted into a better understanding of the slot burner IDF structures in comparison to CoA burners. The flame height was found to be sensitive to the fuel flow rate, increasing proportionally for a fixed air flow rate. For the same conditions the flame height was inferior when compared to a CoA burner, the centerline temperature was greater for the slot burner and the entrainment zone was found to be larger due to the increase in surface area between air and fuel jets as depicted in Figure 1.2(b).

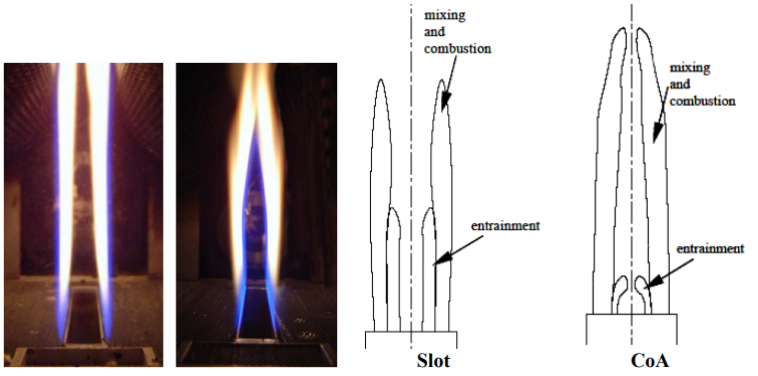

(a) NDF (left) and IDF (right) structure comparison; Source: [8]

(b) Slot and CoA structure comparison; Source: [30]

Figure 1.2: Slot burner structure analysis

In summary, most of the work concerning IDF has focused on flame appearance and structure, flame height, temperature profiles, soot formation characteristics and emissions for mainly CoA and CAP style burners.

1.3 Objectives

The present work intends to study and characterize methane inverse diffusion flames (IDF) in a multi-slot burner. For this purpose it was set out to experimentally obtain a complete global equivalence ratio (ϕ_g) working range of methane IDF for two particular flame powers (fixed fuel flow rate). This was carried

out through the central air flow rate variation. Characteristic flame types are to be analyzed utilizing two particular techniques: flame photography with visual analysis, chemiluminescence spectroscopy and particle image velocimetry (PIV).

The combination of these three techniques will hopefully allow for a quite good methodological structure to characterize the flame morphologies. Flame range photography for the preliminary interest structure identification and the effects of key parameter variations. The chemiluminescence spectroscopy will permit a more detailed measurement of the local equivalence ratio (ϕ), which is particularly useful to understand the mixing phenomena for this type of flame, where the local ϕ are expected to be quite intense due to its inherent diffusive nature. And finally the velocity mappings obtained through PIV will function as an additional window into the inter-jet flow mixing dynamics, isothermal and flame comparisons and also flame velocity profile evolutions.

All the experiments are to be conducted utilizing methane (CH_4) and air, in a multi-slot burner.

1.4 Thesis Outline

This thesis is structured in four chapters. Chapter 1 contextualizes the work by providing an overview of the investigative efforts on inverse diffusion flames and their motivation, from the historical context to the contemporary state of the art and finally details the objectives undertaken in the present work. The following chapter details the experimental methodology, setup and equipment utilized in the laboratory, describing the different techniques utilized and their respective parameters. Additionally the technique-specific uncertainty analysis is presented as well as the general experimental uncertainty common to all. Chapter 3 presents the obtained results and their analysis, contextualized with the previous investigative efforts. The fourth and final chapter summarizes the key findings in the development of the present work. As a final note a number of suggestions for future work are enumerated.

Chapter 2

Experimental Setup, Techniques and Procedures

2.1 Experimental Setup

General Setup

A schematic of the experimental setup used in this work is displayed in Figure 2.1, it was designed in order to maintain control over each flow stream independently, two streams dedicated to fuel and a single central stream dedicated to air, with the properties presented in Table 2.1. To guarantee a proper control of pressure, temperature and volumetric flowrate each fuel line was assigned a dedicated mass flow meter. Methane is introduced into the system from a gas canister, and divided into two separate streams feeding into two digital *Alicat Mass Flow Controllers* with a maximum capacity of 5 SLPM[1] each. Air was introduced through a dedicated line and passed through an air filter in order to remove the water and other impurities before being fed into a third *Alicat Mass Flow Controller* with a maximum capacity of 50 SLPM. All three meters were controlled with a computer utilizing a *LabView* interface, offering individual mass and volumetric flow control over each flowmeter, after this stage all three lines then connected to three independent manual micro-valves leading into the burner through tubular wall-perforated injectors.

In order to minimize air entrainment and room interferences two quartz glasses were attached at both burner slit ends.

Property	Air	Methane
ρ[kg/m^3]	1.276	0.708
$\mu\times10^6$[Pa.s]	17.22	10.24
M[kg/kmol]	28.96	16.04
LHV[MJ/kg]	-	50.01

Table 2.1: Fluid properties at STP. Source: [31].

[1] Standard liter per minute, evaluated at a temperature of 273.13 K and an absolute pressure of 1 bar.

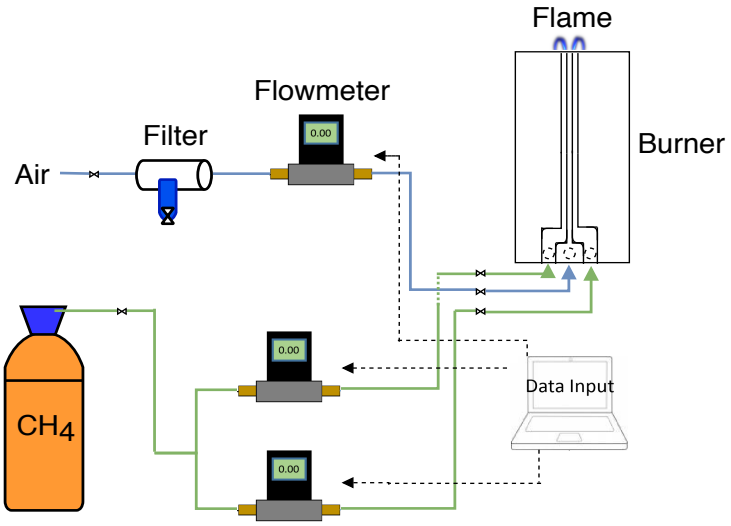

Figure 2.1: General gas feeding and control experimental setup schematic.

Burner Characterization

For the purposes of this work, a two dimensional slot burner with rectangular channels was utilized. In order to characterize IDF under various conditions, this burner was equipped with four 1 mm thick AISI Type 304 Stainless Steel plates arranged in the configuration presented in Figure 2.2, this configuration was chosen to ensure a proper flow development at the burner outlet, which proved quite unstable with a preliminary configuration with converging interior channels and a shorter constant section. The burner has a height of 350 mm, 38 mm slot length and a slot width of 2 mm for all three channels, with a slightly larger injection chamber for both fuel channels due to geometric constraints.

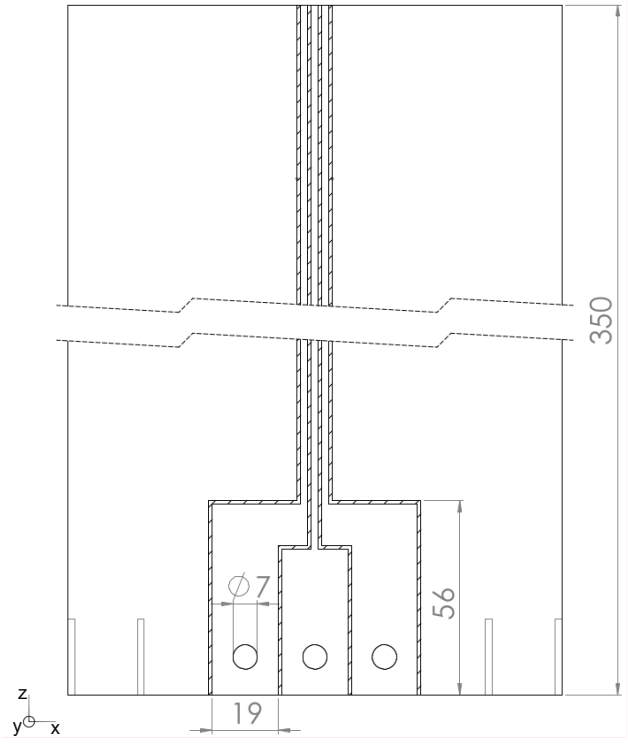

Figure 2.2: Burner cut side view technical drawing (dimensions in millimeters).

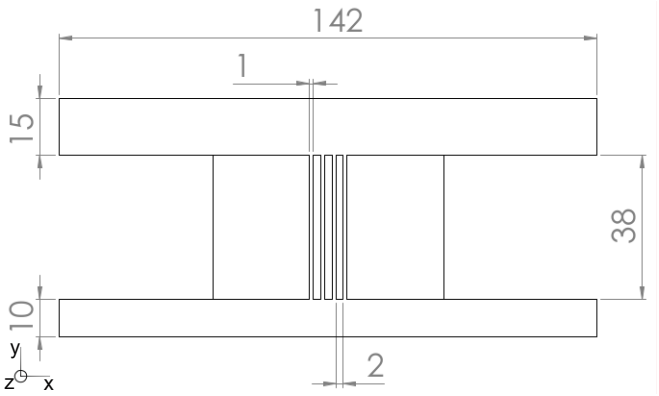

Figure 2.3: Slot burner top view technical drawing (dimensions in millimeters).

An additional improvement was made to the burner with the goal of obtaining a properly stabilized flame with a developed velocity profile. To guarantee laminar flow along the burner slots, all the interior channel curvatures were smoothed through the addition of small neoprene fillets as can be seen in Figure 2.4, reducing the formation of corner recirculation bubbles and the consequent generation of pulsating effects on the flame.

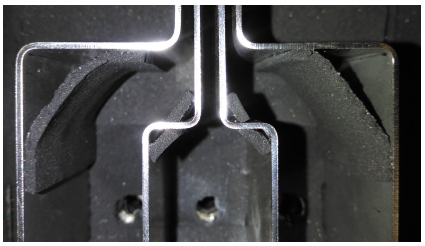

Figure 2.4: Interior injection chamber fillets

It is known that a flow velocity profile inside a rectangular duct under the effect of shear stress, reaches a fully developed state when the boundary layer thickness is equal to half of the distance between plates. The duct length required for this development is denominated transition length, which for a Poiseuille flow in a rectangular duct is given by Equation 2.1 [32].

$$\frac{L_{ent}}{w} = \frac{Re}{5} \tag{2.1}$$

Where L_{ent} is the aforementioned transition length, w the channel width, in this case 2mm and Re the Reynolds number, defined in Equation 2.2:

$$Re = \frac{\bar{U} \times w}{\upsilon} \tag{2.2}$$

where $\bar{U}$ represents the average flow velocity, υ the fluid kinematic viscosity and w the channel width. The transition length was calculated for the velocity range under analysis and the constant slit section length of 294 mm was found to be more than sufficient in guaranteeing a flow fully developed into a parabolic profile at the burner exit for each individual slit, as described by Equation 2.3, with a maximum

velocity of $U_{max} = \frac{3}{2}\bar{U}$ [33].

$$U(x) = \frac{1}{2\mu}\left(\frac{\Delta P}{\Delta X} - \rho g\right)\left(y^2 - \left(\frac{w}{2}\right)\right) \tag{2.3}$$

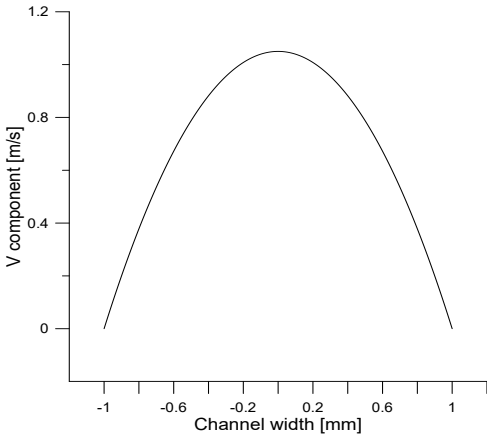

Figure 2.5: Slit theoretical velocity profile for a $\bar{U}$ of 0.7 m/s and a channel width of 2 mm.

2.2 Experimental Techniques

2.2.1 Flame Photography

One important step in characterizing a range of IDFs with this particular burner configuration is the analysis of the flame morphology, and all structural alterations that might occur at different burning conditions. Direct photography was opted to visualize and register these changes. Due to the two dimensional profiles exhibited by the flames, the camera was positioned in alignment with the central air slit.

Experimental Setup and Procedure

For this purpose the burner was stabilized in a fixed position within an aluminium structure aligned with the main camera positioning rail. The surrounding structure was sealed with black panels to improve the photographic acquisition of the pure flame colors without outside light interference. A photograph of this setup is displayed in Figure 2.6.

A *JAI CV-M9-GE, 3-CCD RGB* camera with a resolution of 1074x768 pixels was utilized. This type of camera separates the incoming light into red, green and blue wavelengths, directed to three different sensors, thus providing very accurate per-pixel color characteristics. Additionally, a *Nikon 50mm lens* was coupled to the camera, the images were acquired in *RAW* format with null gain values, 1.6 lens aperture and at a constant fixed distance and alignment for all burning conditions under analysis.

The chosen procedure for the establishment of the flame range subject to analysis, was based on the more prevalent approaches on the study of IDF, as can be seen on a number of the most relevant and recent works [9, 16, 29, 34, 35]. A specific flame characteristic is predominantly utilized, the equivalence

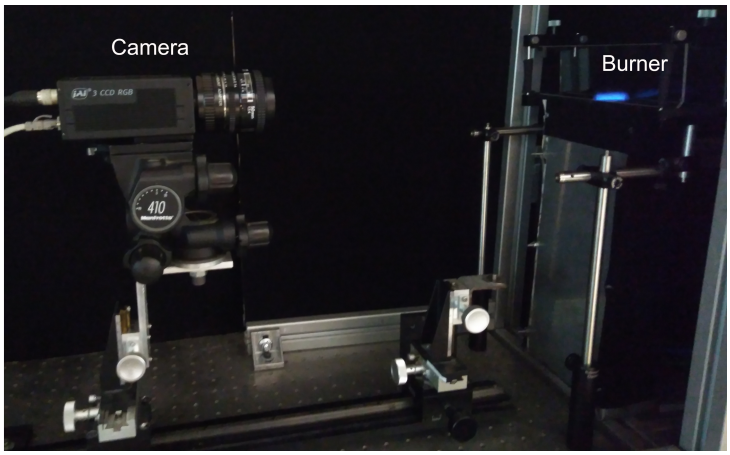

Figure 2.6: Flame visualization setup.

ratio (ϕ), which defines the global ratio between the fuel-to-oxidizer ratio and the stoichiometric fuel-to-oxidizer ratio. It is important though, to bear in mind that this parameter while with clear significance in characterizing premixed flames, where there is a homogeneous mixture of fuel and oxidizer with a determinate ratio. However, it should not be interpreted in the same manner regarding diffusion flames, or for this matter IDF, as the ratio between fuel and oxidizer will be highly variable locally, ranging from regions with 100% to 0% fuel and a stoichiometric flame front reaction center line.

Therefore, for clarity, the equivalence ratio will be denominated as ϕ_g, and interpreted as a global reference based on the input fuel and oxidizer flow rates as defined in Equation 2.4.

$$\phi_g = \frac{\frac{n_{fuel}}{n_{air}}}{\left(\frac{n_{fuel}}{n_{air}}\right)_{stoich}} \tag{2.4}$$

Where $\frac{n_{fuel}}{n_{air}}$ is the actual molar fuel-to-oxidizer ratio and $\left(\frac{n_{fuel}}{n_{air}}\right)_{stoich}$ is the molar stoichiometric fuel-to-oxidizer ratio.

Another important parameter utilized for the flame range characterization was the velocity ratio (Equation 2.5), providing a more immediate perception of the velocities involved and their possible mixing mechanisms and interactions. For clarification purposes a burner slot velocity diagram is presented in Figure 2.7.

$$V_r = \frac{V_{air}}{V_{fuel}} \tag{2.5}$$

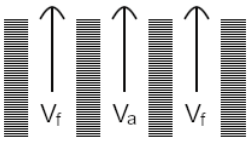

Figure 2.7: Burner velocity schematic

To properly discern the affecting variables, and maintain a flame dimension adequate for visualization, a fixed fuel flow approach was undertaken [9, 10, 14]. Two specific fuel flow rates were fixed (as per Equation 2.6), corresponding to a flame power of 238 W and 455 W.

$$P = \dot{m} \times LHV \tag{2.6}$$

Where $\dot{m}$ is the fuel mass flow rate and LHV is the fuel lower heating value.

2.2.2 Chemiluminescence Spectroscopy

In order to adequately understand and characterize the chemical kinetics in play, an optical technique based on flame chemiluminescence was utilized. This option offered a relatively simple and non-intrusive solution, a very important factor in the study of small scale burning devices, due to the disruptive effects of a thermocouple or probing device when inserted into the flow.

This technique is based on the spontaneous emission of electromagnetic radiation from the chemical species occurring in the combustion process. As an excited radical formed in a reaction goes to its ground state, the emitted radiation will have a specific wavelength and intensity which can be correlated to different flame properties intrinsically related to the setup [36, 37]. The equivalence ratio (ϕ) was the flame characteristic under focus for this work, knowing the band head associated with the peak intensity for the emissions of each relevant radical, namely the OH^*, CH^* and $C_2{}^*$, the subsequent ratios can be calculated, an example of these narrow band peak acquisitions can be observed in Figure 2.8. It has been shown that a correlation to the equivalence ratio can be obtained [38–40] utilizing the three different ratios, OH^*/CH^*,$C_2{}^*/CH^*$ and $C_2{}^*/OH^*$. In particular the OH^*/CH^* ratio has shown to be adequate covering the radiation emitted during lean combustion of methane [38, 41].

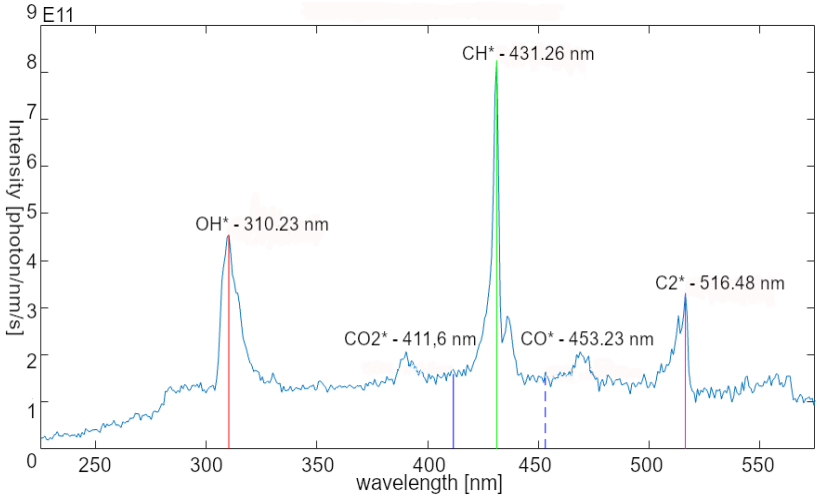

Figure 2.8: Emission spectrum example.

Experimental Setup and Procedure

The setup utilized was composed of a light collecting system consisting of an optical probe arranged with three degrees of freedom in order to adequately adjust the distance to the flame and the sweeping of the flame fronts. A *QP-400-2-SR-BX* optical fiber from *Ocean Optics*, model with a core diameter of $400 \pm 4\mu$m and a solid angle of 25^o, was attached to the spectrometer. The optical probe setup was designed for the collection of light emission in a cylindrical volume aligned with the slots and the two dimensional flames, as depicted in schematic of Figure 2.9.

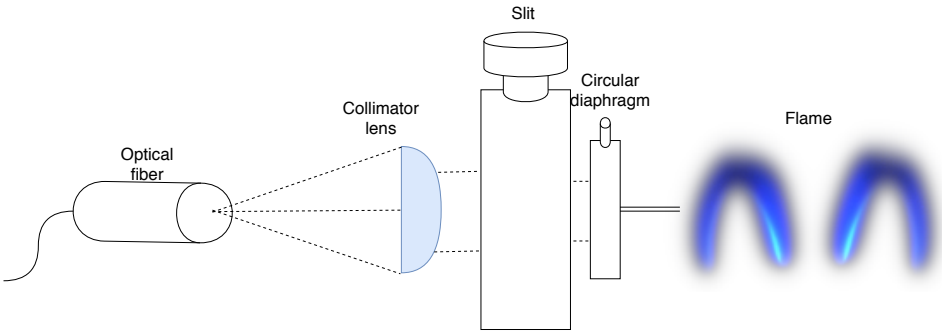

(a) Probe Schematic

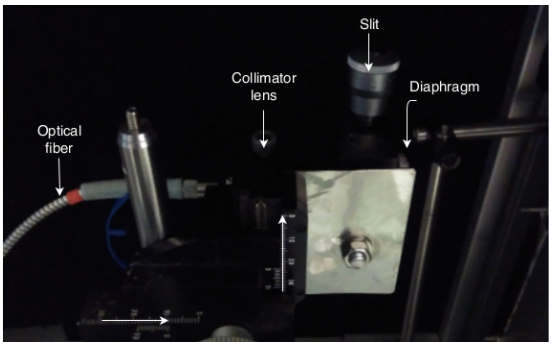

(b) Probe Apparatus

(c) Spectrophotometer

Figure 2.9: Probing Setup.

To do so a collimator lens and two adjustable diaphragms were coupled to the optical fiber, an horizontal slot followed by a circular diaphragm, this way it was possible to limit the area under analysis to a diameter of 0.2mm controlling the amount of light entering the fiber and the spatial resolution. This probe setup is also represented in Figure 2.9

The acquired signal was received by an *Ocean Optics QE65000 Spectrophotometer* with a 200 to 1100 nm wavelength range, the spectrophotometer specifications summary can be consulted in Figure 2.2. The incoming signal was ultimately processed by a computer running the *SpectraSuite* software.

Model	QE65000
Detector	Hamamatsu S7031-1006
Array Type	Matrix CCD
Optical Resolution	$\leq$ 3 nm
Wavelength Range	200-1000 nm

Table 2.2: Spectrophotometer technical specifications.

In regards to the acquisition parameters, with the goal of analyzing the emitted radiation the most accurately and with the least ambient radiation noise contamination possible, 60 individual spectra were acquired with an integration time of 8 seconds each. The multiple spectra were subsequently averaged and the background radiation spectrum was subtracted, this process was done utilizing in-house *MATLAB*® routines.

The main focus of this technique was to obtain the equivalence ratio evolution across the flame of the three different conditions under study, facilitating a better understanding of the structure of IDFs. The

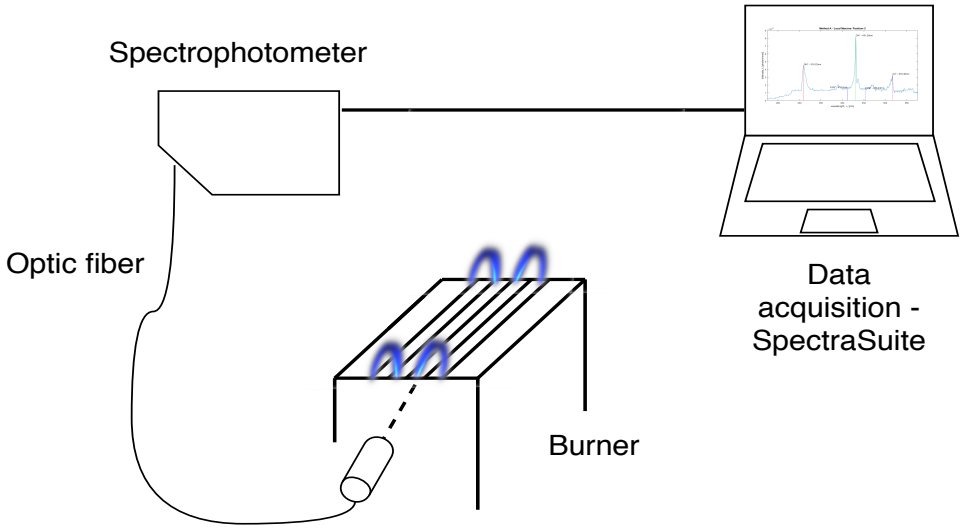

Figure 2.10: Spectroscopy Setup.

intense fuel and air concentration gradients that are inevitably present, their interaction and how they differ for the three flame archetypes under study.

Five horizontal equidistant acquisition points were determined, and their positioning based on the flame visualization previously undertaken. This positioning is depicted in Figure 2.11 for all three flame types and their areas of interest. This idea will be further developed during the flame morphological descriptions in Section 3.1.

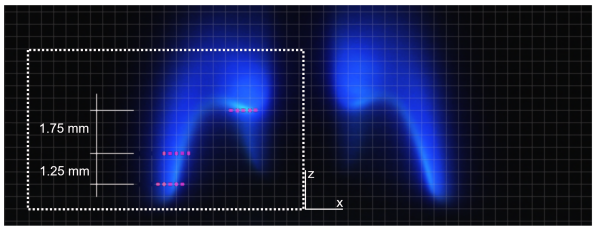

(a) $\phi_g = 0.3$; $V_r = 60$

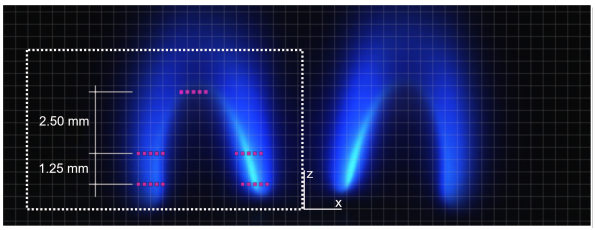

(b) $\phi_g = 1$; $V_r = 19$

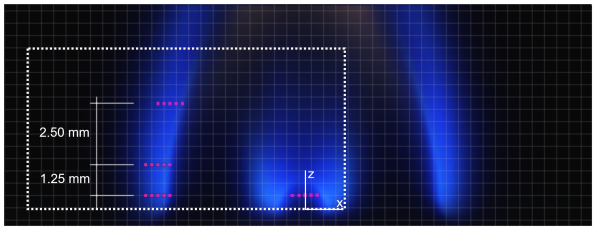

(c) $\phi_g = 3.2$; $V_r = 6$

Figure 2.11: Spectroscope acquisition coordinates. ; $P = 238W$

System Calibration

To correlate the measured values of radical intensity, acquired throughout the chemiluminescence technique to the equivalence ratio, a calibration procedure is essential. Its main goal is to determine an adequate correlation through the analysis of a the radical radiation emissions of a reference flame with

a known equivalence ratio.

As a reference setup, the same slot burner was utilized in a single slot premixed configuration of air and methane as to guarantee a known input of equivalence ratio and power. The flame chemiluminescence was subsequently analyzed for the interior flame blue reaction zone (avoiding the outer plume), in order to obtain the various radical emission intensities for a wide range of equivalence ratios. Ideally, this would be the same range being studied for the IDF configurations, but as previously mentioned, the global equivalence ratio parameter utilized for these diffusion flames is purely indicative of the input proportions. As expected, these values could not be matched with a premixed methane flame. Besides the obtained spectra, a background spectrum was acquired over the same integration time to account for the surrounding radiation emission, and subsequently subtracted from each of the acquired spectra before averaging.

The various radical ratios obtained throughout the whole equivalence ratio under analysis are presented in Figure 2.12.

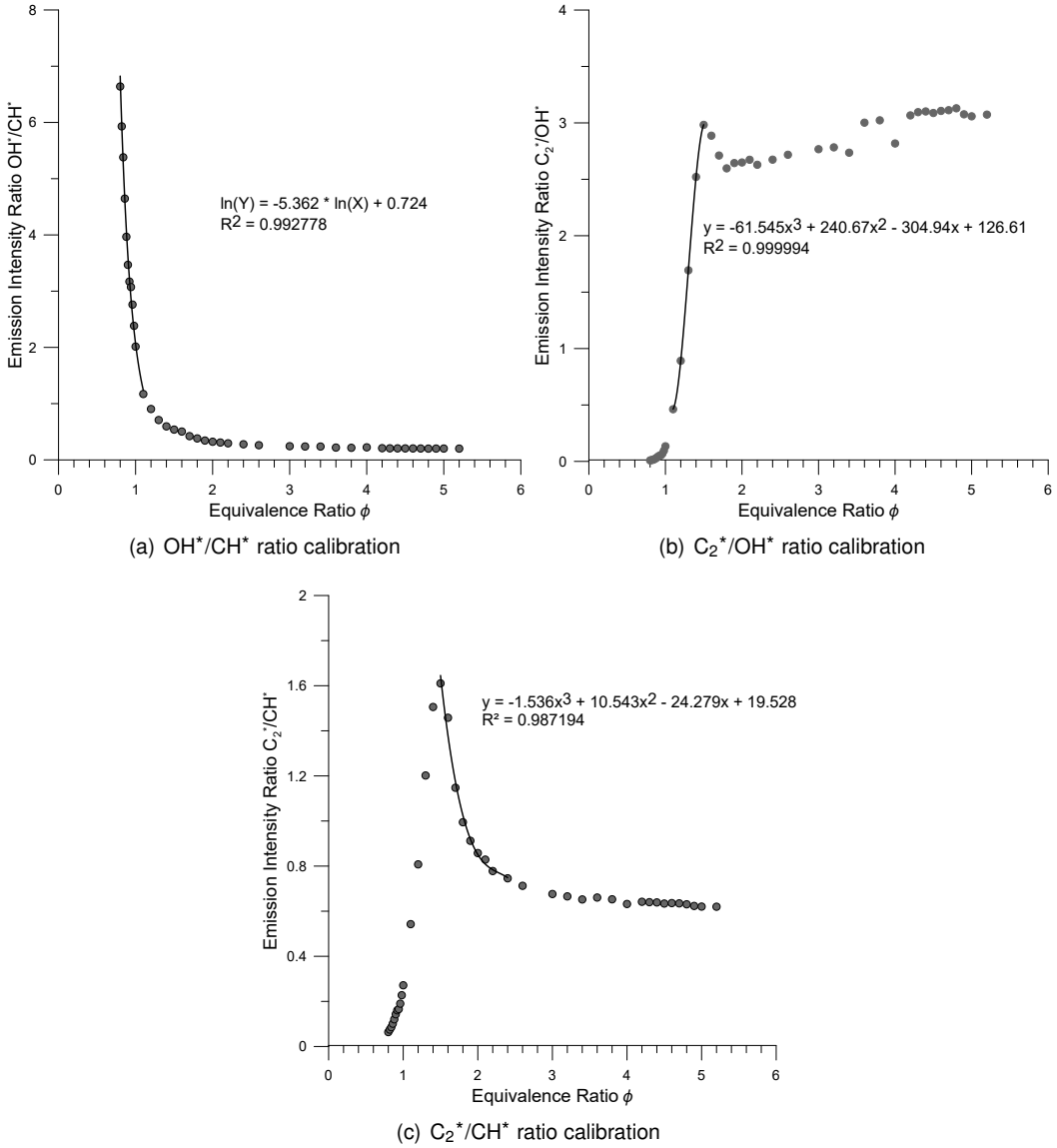

(a) OH^*/CH^* ratio calibration

(b) $C_2{}^*/OH^*$ ratio calibration

(c) $C_2{}^*/CH^*$ ratio calibration

Figure 2.12: Calibration Ratios for ϕ range.

Observing the chemiluminescence ratio curves obtained in Figure 2.12, the differing behaviors exhibit varying sensitivities to the equivalence ratio along its range. Bearing this in mind, the optimum calibration will be a composition of the partial ideal working ranges of each ratio defined by Equations 2.7, and represented in Figure 2.13.

$$\begin{cases} \ln(\phi) = -5.36 \times \ln\left(\frac{OH^*}{CH^*}\right) + 0.724 & 0.8 \leq \phi \leq 1.1 \\ \phi = -61.546\left(\frac{C_2^*}{OH^*}\right)^3 + 240.67\left(\frac{C_2^*}{OH^*}\right)^2 + 304.94\left(\frac{C_2^*}{OH^*}\right) + 126.61 & 1.1 < \phi \leq 1.5 \\ \phi = -1.536\left(\frac{C_2^*}{CH^*}\right)^3 + 10.543\left(\frac{C_2^*}{CH^*}\right)^2 - 24.279\left(\frac{C_2^*}{CH^*}\right) + 19.528 & 1.5 < \phi \leq 2.4 \end{cases} \tag{2.7}$$

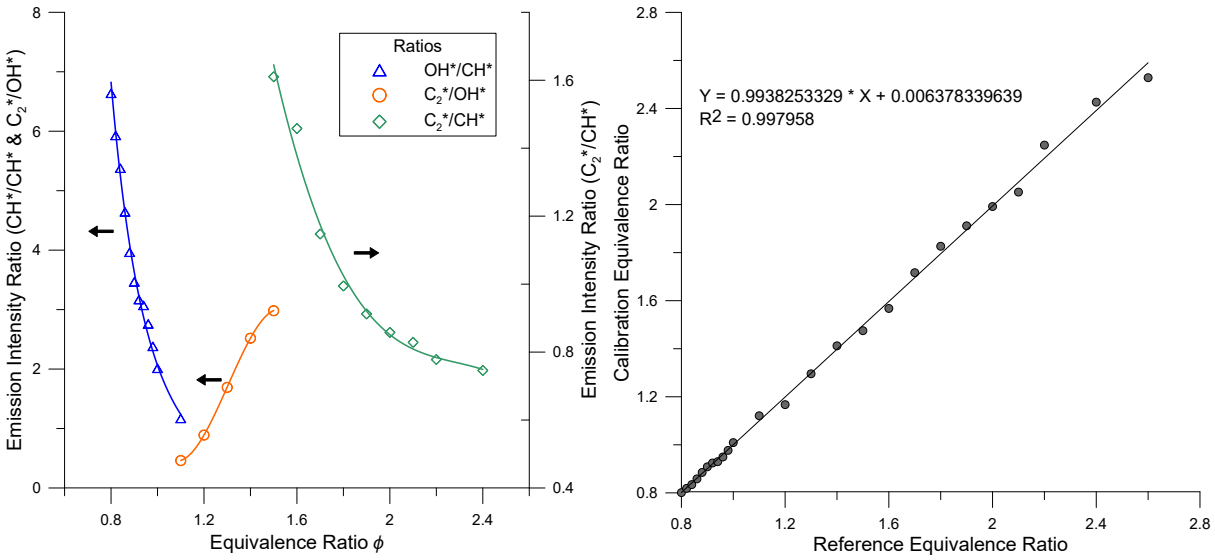

(a) Combined Calibration

(b) Calibration ϕ and Reference ϕ relationship

Figure 2.13: Final combined calibration and comparison to reference ϕ.

This combined range calibration was then applied to the complete range of premixed reference flames utilized in order to confirm the adequacy of the final radical-ratio-based equivalence ratio with the known reference input equivalence ratio. Demonstrating a high determination coefficient (R^2) as can be observed in Figure 2.13

Chemiluminescence Uncertainty Analysis

The measurement of the radicals presents an associated uncertainty, during the acquisition time period, the emission of each radical will have a standard deviation, and this in turn will propagate its effect to the chemiluminescence ratios, therefore altering the values of the equivalence ratios obtained from Equations 2.7.

To account for this uncertainty, the following expressions can be used to estimate the error associated with the three chemiluminescence ratios under use and their error propagation into each equivalence ratio bracket:

$$e^2_{OH^*/CH^*} = \left(\frac{1}{CH^*}\right)^2 \times e^2_{OH^*} + \left(\frac{OH^*}{CH^{*2}}\right)^2 \times e^2_{CH^*} \tag{2.8}$$

$$e_{\phi}^{2} = \left(\frac{\partial \phi}{\partial \left(\frac{OH^*}{CH^*} \right)} \right)^{2} \times e_{OH^*/CH^*}^{2} \tag{2.9}$$

Where OH* and CH* (or analogous radicals) correspond to the average value for these radicals acquired during the total time period and $e_{OH^*}^2$ stand for the errors associated with that specific measurement. These values were acquired for a series of 100 spectra each with an individual integration time of 8 seconds, totaling 13.3 minutes of acquired data

Considering that the calibration procedure utilized a premixed flame, due to the necessity of a known and measurable equivalence ratio, and the flame under study itself was an inverse diffusion flame. To properly characterize the uncertainties associated with the radical detection of each flame configuration, this error calculation was performed for both reference flame and IDF and the equivalence ratio error presented for the reference flame is averaged over the three intervals of the combined correlation equations. The relative errors obtained are presented in Table 2.3.

	Relative error[%]			
	e_{OH^*/CH^*}	$e_{C_2^*/OH^*}$	$e_{C_2^*/CH^*}$	e_{ϕ}
Premixed Reference	2.49	0.23	0.63	6.17
IDF	20.20	4.08	10.81	-

Table 2.3: Chemiluminescence uncertainty results.

2.2.3 Particle Image Velocimetry

Particle-image-velocimetry (PIV) is a quantitative velocity measuring technique. It offers valuable advantages when compared to traditional flow measurement techniques such as the Doppler velocimetry and hot-wire anemometry due to its precision and non-intrusive nature. The flow is undisturbed by probes allowing for a whole-field measurement of the velocity [42, 43].

This technique utilizes small tracer particles inserted in the flow which are subsequently illuminated using a double pulsed laser in the area of interest to produce a green light planar sheet with a wavelength of 530 nm. This laser is synchronized with a high-speed sCMOS camera using a synchronizer connected to the central acquisition system. The camera will acquire two consecutive frames of laser-illuminated particles embedded in the flow under study. The two-dimensional velocity field can then be determined by cross-correlating the two consecutive frames, as well as the time interval between laser pulses and the distance traveled by the seeding particles.

Experimental Setup and Procedure

The setup utilized consisted of five main components: the double pulsed laser, a *Dantec Dual Power 65-15 Yag* with two laser cavities with a maximum laser pulse frequency of 15 Hz each and a wavelength of 532 nm; the image acquisition system, provided by a *HiSense Zyla sCMOS* camera with a framerate of 40 FPS and a resolution of 2560 x 2160 pixels and an added 532 nm filter to protect the camera CCDs and better define the particle light scattering within the flame itself. The synchronization between

these two components was handled by a *BNC 575 Series Pulse Generator*, controlled centrally by an acquisition system on a dedicated computer utilizing the *Dantec DynamicStudio* software

The final component is the seeding system, this setup in particular used 3 separate independent seeding bottles with *Logitech 5 micron Calcinated Aluminium Oxide Powder* particles, in order to assure an adequate and uniform particle density in each channel, in spite of the different flow rates. Two independent electromagnetic stirring and heating plates were utilized, one for the air seeding and one for the fuel seeding, the third and final particle seeding bottle used for the ambient surrounding particles did not require a stirring mechanism due to sufficient particle transport. The setup is represented in the scheme of Figure 2.14.

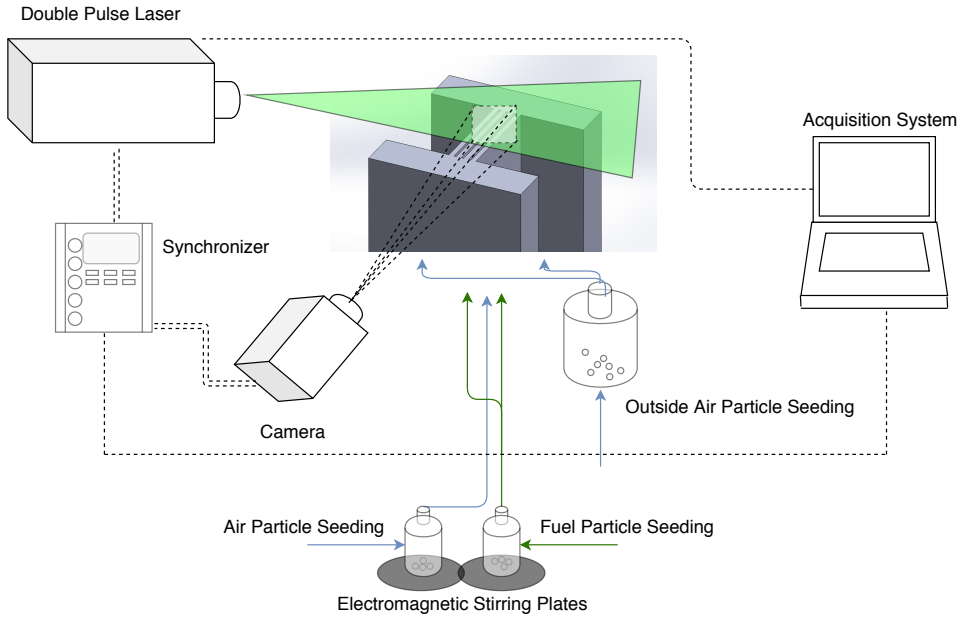

Figure 2.14: PIV Schematic.

One of the main factors to ensure an accurate PIV analysis is the flow seeding, the particle density in the seeded flow must match reasonably with the density of the base flow in order to avoid errors induced by the gravitational effect and maintain the trajectory of the main flow [44]. A number of particle characteristics must be taken into account to guarantee the acquisition of valid data. As described elsewhere [45], the seeding particles must have good light scattering properties. Therefore, they should not be too small, besides they should also be non-corrosive, non-volatile, non-abrasive and non-toxic. Due to this, the aluminium oxide powder is an appropriate choice. Regarding the mean diameter, 3 micron is advised for the use with gaseous flow as described in [44].

In regards to the density of particles in the flow volume itself, the work previously developed [43, 45], provided reference standard images for a number of configuration parameters, as can be seen in Figure 2.15. These references are commonly used in the adjustment of the lighting conditions and particle density.

After stabilizing an appropriate seeding density, the laser focus length was adjusted to the camera field of view center establishing a laser sheet of approximately 1 mm to minimize the associated systematic errors. The camera was kept perpendicular to the laser sheet and aligned with the burner slots at a

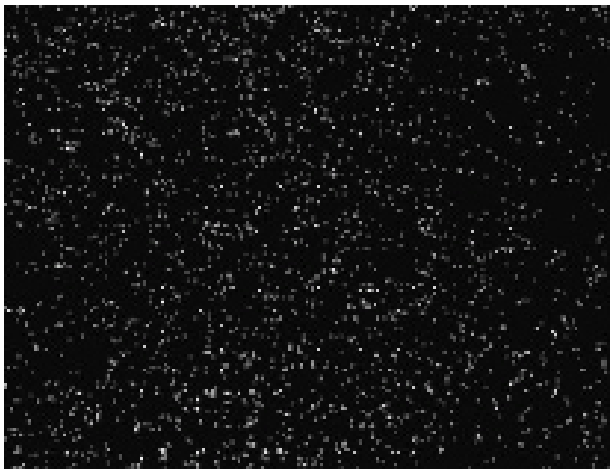

Figure 2.15: Seeding particles density standard.

distance of 15 cm and setup with a *Meller Griot 352 nm filter*.

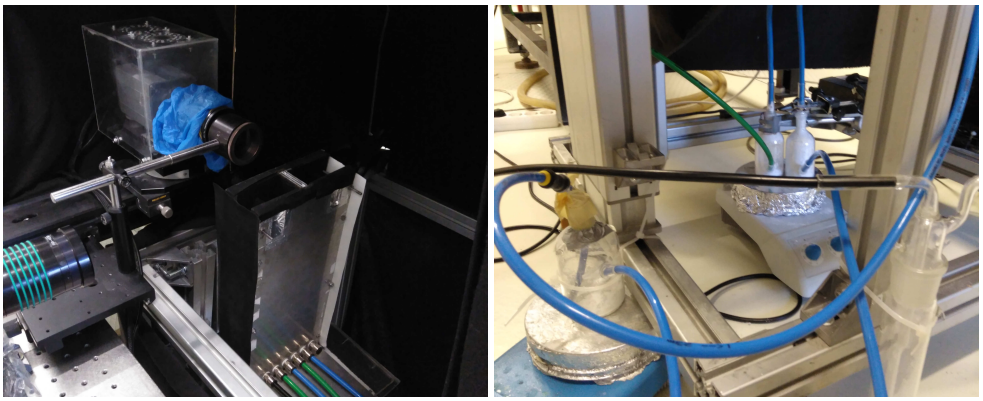

(a) PIV Setup Top-View (b) Seeding Setup

Figure 2.16: PIV Setup.

Post-Processing

The second essential part of the PIV technique is the image analysis. There are a number of procedures that can be done both pre- and post-correlating the acquired particle image pairings. No pre-correlation image filtering was applied, only image masking to limit the area of interest for the analysis.

In regards to correlation methods, there are multiple approaches with different characteristics that better adapt to various kinds of flows and seeding conditions [42, 46]. Cross-correlation is a technique that calculates a 2-D velocity field from an image pair, it is a spatially statistic technique particularly well suited to flow fields with a dominant direction. This approach correlates the light intensity emitted by the particles at the instant of the first exposure (instant t) to the second exposure (instant $t + \Delta t$), in sequence the most probably displacement can be obtained through a peak detection method.

Another possible approach is ”Average Correlation”, where the correlation function of each interrogation area is averaged at each location for all the images. This technique is useful in applications where it can be difficult to maintain a stable particle density during the entirety of the acquisition period, which

was the case with the low velocity ambient particles surrounding the slot flows.

For the flow conditions under study, the average correlation together with the acquisition of a large number of image pairs was chosen over the individual cross-correlation of each pair and final-step vector map averaging.

Another important correlation parameter is the Interrogation Area (IA), which determines the sub-divisions of the main frame into n x n pixels windows as shown in Figure 2.17, which are individually analyzed for both pulses, generating a single mean velocity vector per IA. The chosen dimensions for the IA are linked to the time interval between laser pulses and the distance traveled by the particles during this time window. The three parameters must be such that a clear movement of the particles can be obtained between both frames. If the time between pulses (Δt) is too small, the particle may have a smaller displacement than necessary to properly obtain a velocity vector, therefore, for a constant IA dimension, a small Δt would be adequate for a flow with a high velocity. The opposite will be true for a low velocity flow, as the high velocity particles could exit the IA under analysis if Δt is too high. Bearing in mind all these precautions the particles captured close to the IA borders can still be lost to the outside between frames, this can happen even under adequate parameters of Δt and IA dimension. Therefore, a third parameter must be taken into account during the correlation, the overlapping factor approximates neighboring IAs allowing the existence of more vectors in both on-plane directions, to account for this loss of information an overlapping factor of 50% x 50% was utilized.

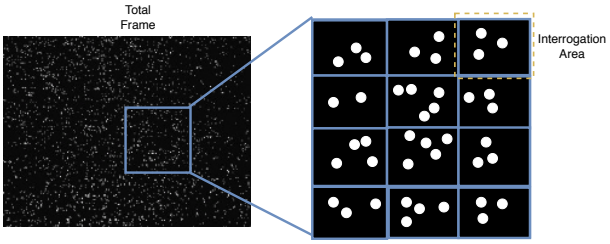

Figure 2.17: Interrogation Areas subdivision schematic.

Parameter	Option
Image pairs per recording	200
IA size	32x64 / 64x128
Time between pulses	60 μs / 200 μs
Correlation technique	Average Correlation
Overlapping factor	50% x 50%

Table 2.4: Summary of PIV parameters

As an additional note, one factor that must be kept in mind during this analysis, is the three dimensional-effects that can be present due to the flow nature, the occurrence of an out of plane particle movement can cause a sudden absence of particles between frames. For some cases, this can be compensated for with a laser focus length adjustment, providing a thicker laser-sheet. Nevertheless, this will introduce the erroneous perception of a 2-D displacement. Due to this, this effect is not prominent in the type of flow developed in this type of burner and flame, and the laser sheet thickness was maintained at a

minimum for the area under analysis.

PIV Uncertainty Analysis

In order to analyze the uncertainty associated with the PIV velocity measurements, the theoretical velocity profile for the burner slots presented in Figure 2.18 for a channel width w of 2 mm and an average velocity of 0.70 m/s (corresponding to $\phi_g = 1.2$) can be taken as a representative work base for the velocity uncertainty analysis. As previously mentioned, the fully developed flow exhibits a parabolic profile, the theoretical prediction was plotted against the values obtained during the PIV analysis for a single central slot air flow with $\phi_g = 1.2$. The sample standard deviation was computed over 6 correlations of 50 image pairs taken for an IA size of 64x128 and a pulse interval of 200 μs.

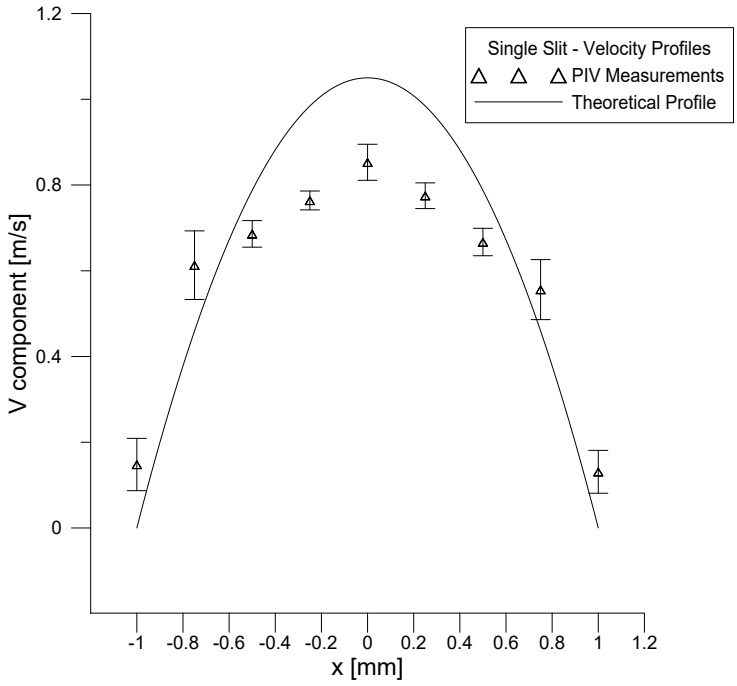

Figure 2.18: PIV velocity uncertainty analysis for an average exit velocity of 0.70 m/s.

The root mean square error (RMSE, equation 2.10) between the average PIV and theoretical values was computed, showing a value of 0.161 m/s, which relative to the center line velocity of the same theoretical profile, shows a 15.3% discrepancy.

$$RMSE = \sqrt{\left(\frac{\sum_{i=1}^{n}(P_i - O_i)^2}{n}\right)} \tag{2.10}$$

Despite the laminar nature of the flow, small local fluctuations in velocity are to be expected. This can be due to room interference, burner imperfections or particle seeding density inconsistencies, therefore the error bars associated with this experimental error are also represented in Figure 2.18. The maximum PIV velocity value fluctuations (41%), found to occur closer to the slot edges, can be associated with the boundary layer effect at the interior burner slot walls. For the entirety of the profile, the average deviation obtained was 14%.

2.3 General Experimental Uncertainty Analysis

Flow Meter Uncertainty

As stated in the experimental setup, the flow rate control was assured with the use of digital mass flow meters. These equipments have an inherent uncertainty, which should be quantified in order to properly control and validate the experimental method utilized. The meters present uncertainty values associated with both reading $(\pm 0.8\%)$ and scale $(\pm 0.2\%)$. Therefore the flow meter uncertainty can be calculated using the following general formula:

$$e_Q = 0.008\bar{Q} + 0.002Q_{max} \tag{2.11}$$

where Q is the range of operating flow rates utilized and Q_{max} corresponds to the maximum flow rate of the specific meter utilized for each range. To minimize the scale errors each meter was chosen with the minimum capacity possible for each of the streams and their desired flow rates. These values can be verified in Table 2.5

Input Range $\bar{Q}$ [SLPM]	Flowmeter Q_{max} [SLPM]
$0.025 \leq \bar{Q} \leq 5$	5
$5 \leq \bar{Q} \leq 20$	20
$20 \leq \bar{Q} \leq 40$	50

Table 2.5: List of utilized flow ranges and corresponding equipment maximum.

Furthermore, the effects of these flow rate uncertainties will be propagated throughout the experimental method, influencing the main combustion properties and conditions under analysis, namely the global equivalence ratio (ϕ_g) and the burner exit velocities (U_A and U_F referring to air and fuel respectively), to properly account for this error propagation, equations 2.12 and 2.13 were utilized [34], and the corresponding relative error values for each component of the flame regimes under analysis are presented in Table 2.6.

$$e_\phi^2 = \left(\frac{\partial \phi}{\partial Q_F}\right)^2 e_{Q_F}^2 + \left(\frac{\partial \phi}{\partial Q_A}\right)^2 e_{Q_A}^2 \tag{2.12}$$

$$e_U^2 = \left(\frac{\partial U}{\partial Q_F}\right)^2 e_{Q_F}^2 + \left(\frac{\partial U}{\partial Q_A}\right)^2 e_{Q_A}^2 \tag{2.13}$$

	Relative error[%]				
	e_{Q_A}	e_{Q_F}	e_ϕ	e_{U_A}	e_{U_F}
$\phi_g = 3.2$	1.63	1.65	4.91	1.89	0.36
$\phi_g = 1.0$	1.06	1.65	5.47	2.32	0.36
$\phi_g = 0.3$	1.05	1.65	5.77	1.67	0.36

Table 2.6: Relative error values associated with the three main conditions under study.

As can be verified in Table 2.6, in regards to the three main flames under study, the relative error

presented an acceptable maximum percentage for each property. The error analysis for the complete range of burning conditions utilized in the morphological characterization can be consulted in Appendix B, Section A.1.

Chapter 3

Results

3.1 Flame Morphology

As with normal diffusion flames (NDF), the visual appearance, both in terms of structure and luminosity, of IDF is dependent on the stoichiometry, flow velocity fields of fuel and air, burner geometry and fuel type [5]. To gain insight into the working range, stabilization mechanisms and flow interactions of the IDF in a multi-slit burner, it was important to discern the effects of each parameter, therefore two different fuel flow rates, and respective flame powers, were fixed. Isolating in this way the effects of the velocity ratio, V_r (through the increase of air flow rate) and consequently the global equivalence ratio (ϕ_g) variation.

Between both flame powers, four distinct types were visualized across the entirety of the range tested: Type I is characterized by the triangular shape of the flame front; Type II presents a transition structure, where an inner flame front is generated but a disconnect is maintained with the outside flame fronts; Type III is characterized by the continuous symmetric flame fronts separated by the air jet, and finally Type IV, where the interior flame fronts rise and stabilize in a ”neck-like” structure. Let us now proceed with a more in-depth analysis of each flame type. For illustrative purposes, the three independent channels are represented with colored arrows in all pictures with green corresponding to fuel flow and blue to the central air flow.

Flame Type I

This type of flame is present in the richest part of the range, starting at the purely diffusion flame utilizing only ambient air, up to a flame (now with central slot air jet with $V_r = 2$) presenting a value of $\phi_g = 9.5$. The flame structure does not show any luminous interface between the injected air and fuel jets, only between the fuel jets and outside air. This is due to a diminished between-jet interaction, thus the flame behavior is closer to a buoyancy driven diffusion flame with a conical structure formed due to flame stretching effect , as described in [21, 31]. Two distinct flame regions can be identified, a blue region and a yellow one. This second, almost entirely encapsulated in the interior of the blue flame front.

These regions demonstrate the duality of the IDF, with the presence of an intense reaction zone

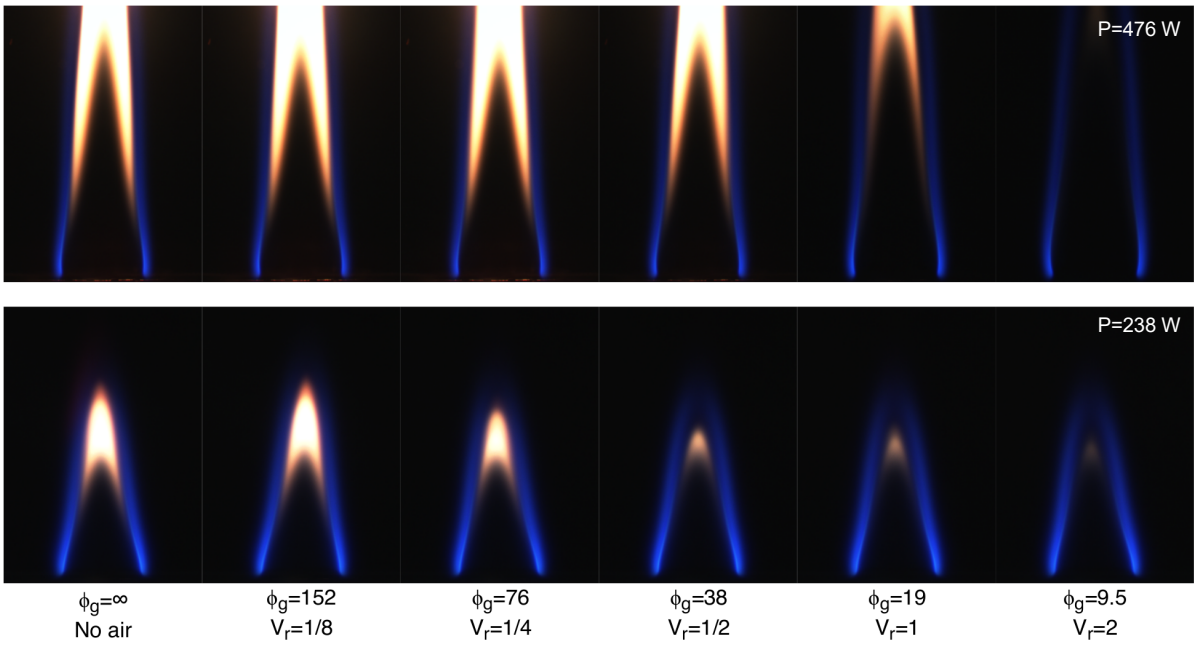

Figure 3.1: Type I flame range.

where the mixing is much more substantial and no soot is produced, followed by a diffusion combustion zone as previously detected in other studies [5, 14, 20, 27, 35, 47].

The presence of a yellow region is indicative of soot formation, associated with incomplete combustion caused by a local excess of fuel, which is characteristic of diffusion flames. This area has an inverse "V" shape, which is expected due to the presence of the two symmetrical jet flows at both sides, causing the yellow zone to start earlier upstream close to the flame fronts, only later connecting downstream at the tip. This zone diminishes progressively with the decrease of the global equivalence ratio induced by the increase of the central air flow rate. It is important to note that the flame height slightly decreases in this range, mainly due to the increased local reaction rate. A reduction in the yellow-emitting zone is also visible caused by a progressively leaner air-fuel mixture, not only globally, but locally.

Figure 3.2: Type I flame interest zones ($\phi_g = 38$; $V_r = 1/2$; $P = 238W$).

This reduction of the luminous zone can be explained with the help of relative velocity and momentum between fuel and air jets. The increase in air velocity causes an increase in shear between air and fuel, enhancing the mixture between them upstream. This intense mixing zone has been identified in numerous studies, and its size is inversely proportional to V_r [16]. This is to be expected as, due to the intense pressure gradient, the area required for this mixing to occur is shortened because the fuel jet impingement occurs immediately at the burner exit [16, 27, 35, 47].

Regarding the encapsulating nature of the blue region accompanying the yellow tip, as shown by

K.S. Ha in [48], partially premixed methane NDF presented this enveloped feature, yellow inside and blue outside. The same was observed by Shaddix et al. for slot burner NDF in [8], but in contrast the same study found an inversion of these layers for IDF (although with a power one order of magnitude greater than the present study), related with the presence of policyclic aromatic hydrocarbons (PAH), which are byproducts indicative of an incomplete combustion conducive to the production of soot, and OH (blue reaction zone).

Bearing in mind these findings, let us look at the subsequent work developed by Mikofski et al. [10]. With concentric burner methane IDF, it was found that the luminous soot zone only obscured the OH contour for a flame with a height greater than 10 mm. Therefore, this encapsulating blue layer effect shows that additionally to the dual IDF structure, there is an upper flame front layer organization characteristic of a partially premixed NDF, possibly associated with the quite low fuel flow rate utilized (bearing in mind the absence of a substantial difference in V_r between both studies), which would be in line with the connection to a shorter flame [10] and, a lower power [8].

Flame Type II

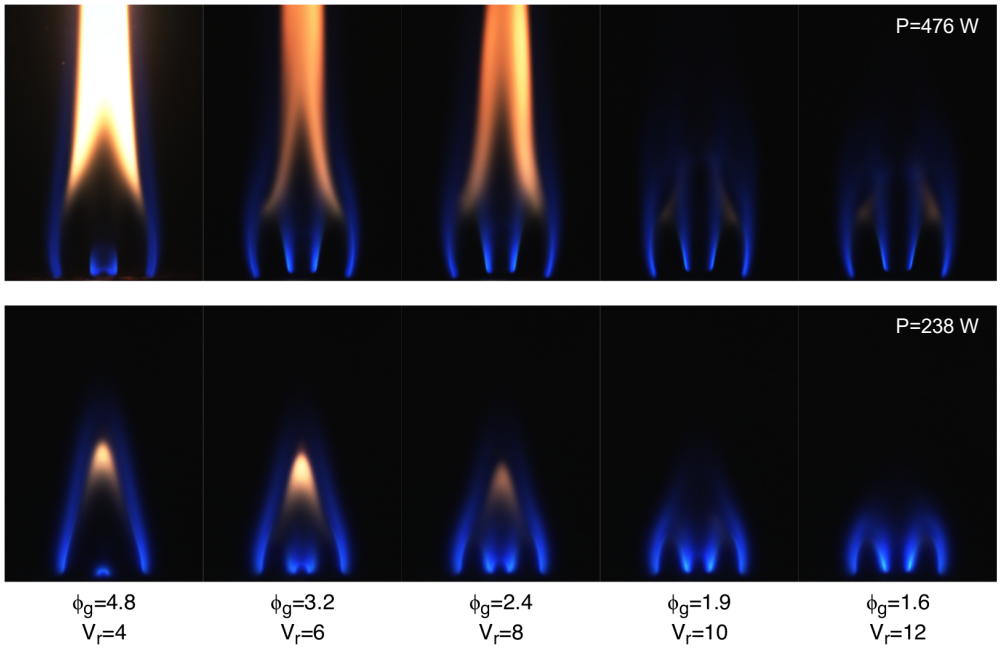

Figure 3.3: Type II flame range.

The second type of flame is identified in the $4.8 \geq \phi_g > 1.9$ range. It is characterized by one main phenomenon, the appearance of a smaller interior flame front over the central air slot. As the air flow rate is increased and the soot production zone is eliminated, the amount of oxidant reaches a critical point where this interior flame stabilization is possible. This double-layer blue flame structure has been observed by Hamins et al. [49] and Huang et al. [50] for double concentric jets. This is accompanied by a sudden reappearance of the yellow luminous tip zone, which is to be expected due to the depletion

of oxygen happening downstream caused by the newly ignited upstream flame front, close to the air channel exit, further exacerbating the fuel rich soot generation area near the flame top.

As this morphological regime shifts towards a leaner global equivalence ratio, the small incipient inner flame begins to move towards the preexisting outside flame front. This is where a quite significant height decrease becomes evident, along with a reduction of the yellow luminous zone. The effect is particularly substantial for the 476 W flame, as seen in Figure 3.3, this phenomenon will be further discussed in an upcoming sub-section dedicated to flame height analysis.

As the interior flame front connects with the exterior one, two symmetric structures start to form, with two distinct tips, a total absence of a yellow zone, and a clear blue intensity increase in the flame front interfaces with the air jet. This intensity increase can be associated with the much more intense mixing occurring at the air jet/fuel jet interface than in the ambient air/fuel jet one. Although outside air entrainment exists, the velocity gradient and shear between both jets is much greater, leading to more intense mixing.

Figure 3.4: Type II flame interest zones ($\phi_g = 3.2$; $V_r = 6$; $P = 238W$).

Flame Type III

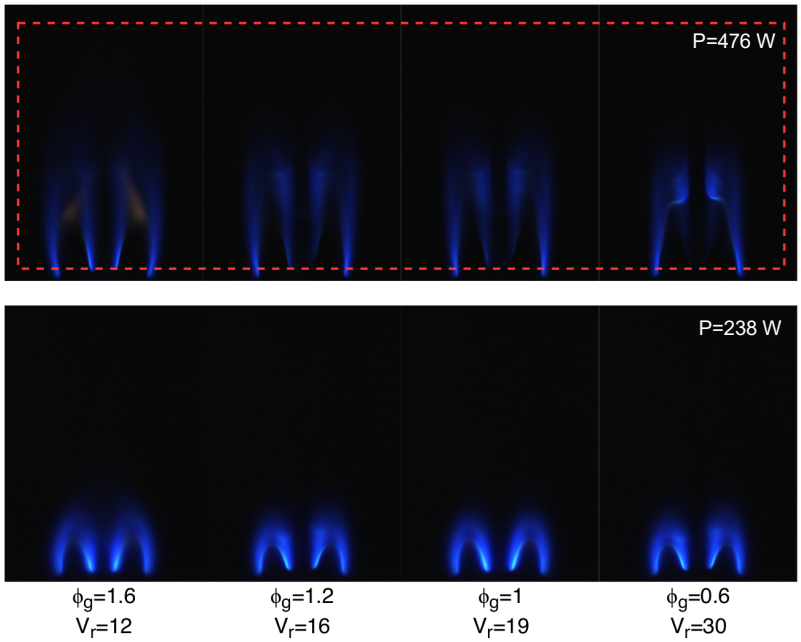

Figure 3.5: Type III flame range. Transitional flame morphology highlighted in dashed line for the 478 W flame.

The third morphology ranging $1.9 \geq \phi_g > 0.4$ features a double structure arrangement, that can be seen as two interdependent flame fronts feeding from the same central air jet. As all previous flame types, these are structurally symmetrical in relation to the central air axis but, without the formation of

any flame front in the direct pathway of the central slit, as shown in more detail in Figure 3.6. Once again, the intense blue mixing zone is present on both inner flame fronts and there is a progressive height decrease towards the leaner range.

This structure has been observed in lean IDF by Abdelaal et al. [30] for a similar slot burner configuration with equal cross-section channels, but has not been previously reproducible in any of the concentric configurations.

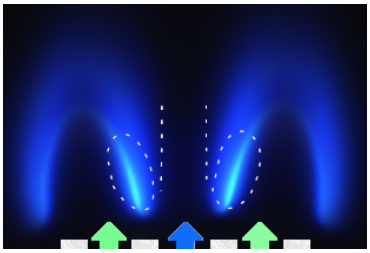

Figure 3.6: Type III flame interest zones ($\phi_g = 1$; $V_r = 19$; $P = 238W$).

It is important to note that for the higher powered flame analysis, this stable regime is never achieved (as delineated in dashed line in Figure 3.5). There is a preservation of a double yellow tip further into the lean parameters and as they dissipate, an unstable range where the interior flame fronts are unable to attach at the base is evident. At this stage the conical shape is completely destroyed because of the weakening of the flame stretch effect caused by the increasing entrainment of surrounding air, and inter-jet mixing [21]. This yellow tip buoyancy-induced flickering was referred in [51], where the presence of these yellow plumes was attributed to the buoyant acceleration of the hot gases outside the diffusion outer flame layer, causing shear-layer roll-up and the formation of vortexes. This oscillatory behavior is only dissipated at $V_r = 30$ as the flame transitions into Type IV. Therefore, it can be considered that this stable flame configuration was not obtainable for the higher fuel flow rate condition.

Flame Type IV

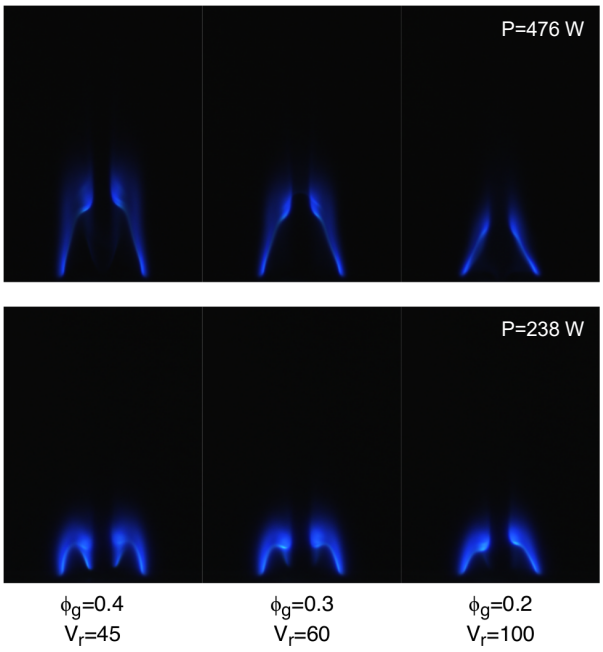

Figure 3.7: Type IV flame range.

The fourth and last flame type identified in the more extreme lean range of $0.4 \geq \phi_g \geq 0.2$, is characterized by the return to a configuration without interior attached flame fronts. These have risen to form a ”neck-like” structure at the flame top, split by the high velocity air jet, with a $V_r \geq 45$. This neck structure generation was identified by Dong et al. for a CAP burner to be triggered for $Re_{air} = 300$ [21]. Let us now, for comparative purposes, utilize the Reynolds number formula described in the previous chapter with the slot width as a reference dimension. With this definition the equivalent transition occurs at $Re_{air} = 355$ for the 238 W flame and about $Re_{air} = 450$ for the 476 W one, thus it can be concluded that for these two burner geometries the formation of a neck-like structure was present at approximate Reynolds numbers, with a slight delay for the higher powered flame. It is important to note the slight blue zone delineated by yellow stroked line in Figure 3.8 is a superposition of a slight flame front downward deflection occurring at the slit half span.

A highly luminous intense reaction zone can be observed in the neck curvature. Analyzing the work previously developed utilizing CAP burners, it was observed that the increase in the air Reynolds number, and consequently V_r, led to increased entrainment of the outer fuel jets into the inner air jet due to a larger pressure gradient. This phenomenon produced approaches a cross flow, forming a structure described as a flame ”neck”, which functioned as a mixer and holder for the upper flame torch for these burner types [12, 18, 20]. Sze et al. [13] has also reported this zone as reaching the highest temperature, indicating that the most intense combustion occurred in this part of the flame. Associating these previous observations with the knowledge that the OH concentration reaches a maximum near the position of maximum temperature [10], the intensely reactive blue neck region found in the flame type under study, can be considered as an analog to the neck constrainment found in CAP burner IDF.

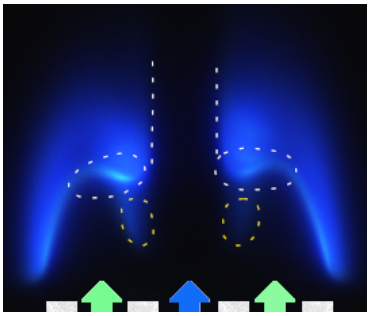

Figure 3.8: Type IV flame interest zones ($\phi_g = 0.3$; $V_r = 60$; $P = 238W$).

This flame type is characteristic of a momentum-controlled flame, being that the main difference between this type of IDF and a buoyancy-driven partially mixed IDF is the absence of an inner flame layer [20]. For this and the Type III case, no inner flame layer is attached to the air jet exit. This is due to the increased quench effect of the cold air jet when Re_{air} and equivalently the air flow rate is sufficiently high [15, 21]. Additionally, it can be conjectured that the presence of this necking zone near the flame base of the IDF plays an important role in destabilizing the flame from the burner rim. Due to the progressive height reduction associated with the air flowrate increase, the neck region will approach the flame base, and tear due to the local strain rate increase resulting in the blowout of the IDF as previously observed by Mahesh et al. in [27].

3.1.1 Flame height

Concerning the determination of the flame height, the most common method is visual inspection [52]. However it quickly becomes apparent that due to the dramatically different flame morphologies across

the range, the direct measurement of the visual flame length would not be a well suited approach, in particular due to the fuel-lean flame neck structures. In spite of this, one of the single most corroborated observed behaviors of the IDF is evident, the general decrease in flame height with the air velocity increase. This is due to the mixing improvement and shortening of the entrainment zone and consequent increase of the partial premixed upstream combustion regime [9, 14, 16, 27, 35, 53].

One important observation can be made in regards to this flame height reduction. In contrast to the majority of the studies that found a roughly continuous decrease, it is evident that there is a sudden transition at the moment of a double symmetric structure definition. This can be seen to occur at $V_r = 10$, causing a considerable visual flame height reduction for the 476 W flame as shown in Figure 3.9. This behavior has previously been reported by Elbaz et al. for a CoA burner [53], this discontinuity was detected around $V_r = 15$, which relatively to the wide range under analysis shows quite good accordance to the behavior observed in the present work.

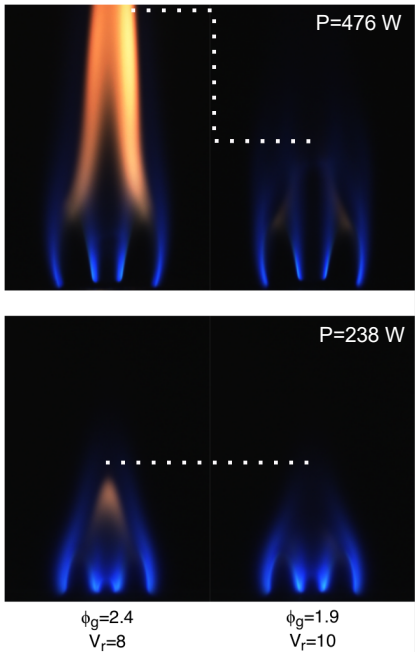

Figure 3.9: Visual flame height discontinuity.

In general, the power increase resulted in an increased flame height for all regimes as previously observed for a slit burner elsewhere [30].

3.1.2 General morphological considerations

In summary, the structure duality of an highly intense entrainment zone upstream (reminiscing a partial premixed configuration) and a downstream diffusive burning regime was verified, with the air-fuel jet interference caused by the velocity ratio between both flows (and consequently a pressure gradient) as the main driving force in the determination of the flame structure and the flow pattern. Through the control of the air flow rate, V_r, Re_{air} and ϕ_g were varied for two fixed fuel flow rates, leading to the identification of four different flame types with distinct characteristics. To further illustrate the dramatic

structural changes caused by this combination of flame shortening and entrainment increase, the flame front center lines for all four flame types (with one representative flame for each) are delineated as well as the yellow soot zones, when present, in Figure 3.10. These four representative flames were chosen according to their well-defined structures, representing a middle of the range representative flame for each of the types under consideration.

The burning conditions ranged from a fuel-rich extreme with a pure diffusion combustion regime, to a lean blowout limit of $\phi_g \geq 0.2$. It was verified that the lean blowout limit is not affected by the fuel flow rate, as previously shown by Zhang et al. for a CoA burner [54]. Additionally, it was observed that the blowout of the IDF occurs without significant liftoff in comparison to the transition from an attached flame at lower V_r, to blowout occurring via a high V_r lifted flame for NDF [55, 56]. Indicating that the early upstream flame region is helping to stabilize the flame. But as the neck constrainment travels further upstream, this mixing zone shortens, as previously mentioned, up to a critical $V_r = 100$ (see Figure 3.7), at this moment the local strain rate around the neck causes the flame to tear and suddenly blowout in the absence of any upstream liftoff [27, 53].

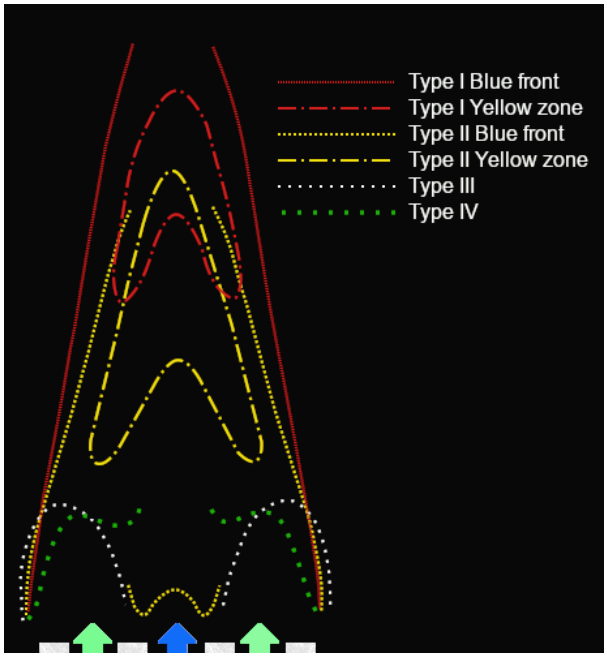

Figure 3.10: Combined flame front overlay.

In an effort for a more in-depth understanding of the mechanisms governing the flame type behaviors previously detailed, three main characteristic flame conditions were considered as representative of each relevant flame type for the chemiluminescence and particle image velocimetry analysis. Namely the morphologies for which the flame behavior is most differentiated from the thoroughly studied normal diffusion flame.

Therefore, the three reference flame types were II, III and IV, under the burning conditions detailed in Table 3.1.

Flame type	ϕ_g	Air flow rate [SLPM]	V_r	Re_{air}	Power [W]
Type I	38	0.1	0.5	6	238
Type II	3.2	1.2	6	35	238
Type III	1	3.8	19	112	238
Type IV	0.3	12	60	355	238

Table 3.1: Summary of Chemiluminescence and PIV burning conditions.

3.2 Flame Chemiluminescence

As a preliminary approach, before proceeding with the local spectroscopy, the three reference flames were analyzed utilizing a non-intrusive technique developed by Araújo [57], based on the processing of flame images acquired with a charged coupled device (CCD) camera utilizing an equivalence ratio analysis algorithm. This algorithm is based on the correlation of specific descriptors associated with the ratios between each individual color channel, red, green and blue, and the local equivalence ratio attributed to each pixel. This technique requires an additional calibration database, which was obtained for a premixed methane flame utilizing the same burner as in the current work. This technique was evaluated for $0.65 \geq \phi \leq 1.2$, in spite of demonstrating a reduced sensitivity for the fuel-poor range, it is still proven useful for a qualitative analysis of the gradients for the range under consideration. Therefore, the application of this methodology provided a comparative reference for the chemiluminescence spectroscopy and a case-study for the validation of the numerical algorithm.

3.2.1 Image Processing Analysis

For all three flames symmetry along the central air jet axis is conserved. Therefore, to minimize the computational processing time required, the analysis was applied to the left side of the flame. The results obtained are presented as an overlay on the flame image.

Type II

The following results were obtained for the Type II flame ($\phi_g = 3.2$; $V_r = 6$)

As expected, due to some algorithm limitations, the analysis of the yellow-emitting region is non-indicative of a definite local equivalence ratio and presents a substantial amount of noise interference due to the soot black body spectral emission.

Considering the two interest zones for this analysis, the inner and outer blue flame fronts, Let us start with the analysis of the exterior flame front of this Type II flame. A yellow close to stoichiometric reaction zone was clearly detected along this front, with a notable size reduction downstream towards the flame top. This can be correlated to the previously mentioned inverse "V" shape of the yellow region. The excess fuel that is progressively reducing its interaction with the exterior flame front as it travels downstream, is the precursor for the formation of the yellow region.

In contrast, the interior smaller flame front presents a substantially fuel-richer reaction zone indicative of a more accentuated fuel movement towards the central air jet. It can also be observed that this rich

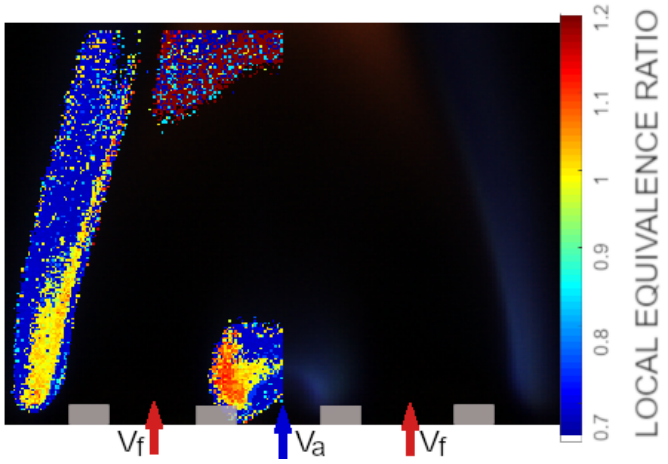

Figure 3.11: Local equivalence ratio results of flame Type II ; ($\phi_g = 3.2$; $V_r = 16$; $P = 238W$).

region is constrained to the fuel-air interface, as the upper part of this small interior flame presents a stoichiometric reaction line delimited by fuel-lean (blue) regions.

Type III

The following results were obtained for the Type III flame ($\phi_g = 1$; $V_r = 19$)

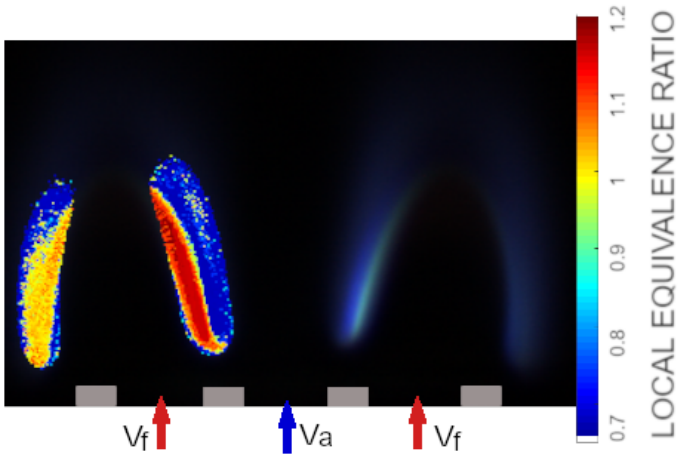

Figure 3.12: Local equivalence ratio results of flame Type III ; ($\phi_g = 1$; $V_r = 19$; $P = 238W$) .

For this case, a stark contrast between the interior and exterior flame front can be observed, in particular the absence of a quite rich red zone on the fuel-side exterior flame front in comparison to its interior counterpart. This could be due to the fuel movement towards the interior air-fuel interface caused by the higher velocity gradient, resulting in a wider stoichiometric (yellow zone) for the exterior flame front. Another notable detail is the presence of an exterior leaner flame front region upstream towards the burner exit, indicating the existence of outside air entrainment close to the flame base.

Type IV

The following results were obtained for the Type IV flame ($\phi_g = 0.3$; $V_r = 60$)

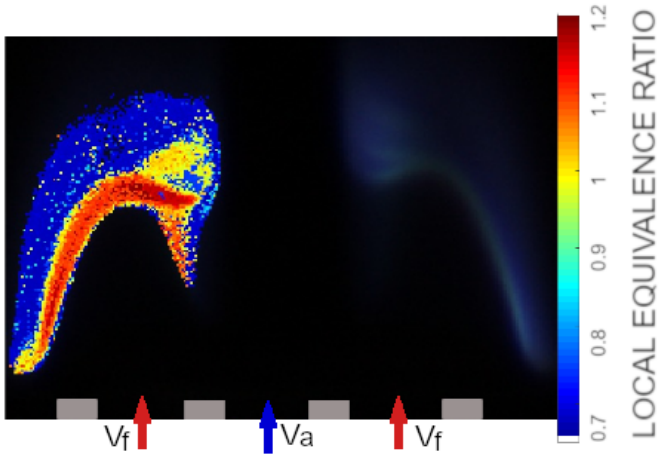

Figure 3.13: Local equivalence ratio results of flame Type IV ; ($\phi_g = 0.3$; $V_r = 60$; $P = 238W$).

For this third and final case, the numerical algorithm detected the entirety of the flame front, with a clear local equivalence ratio gradient. As expected for a diffusion flame, the existence of a zone presenting close to stoichiometric conditions, is clear. This thin zone is surrounded by an interior rich zone (red color) on the fuel jet side, and a lean zone (blue color) on the ambient air side.

The most notable result for this flame type is the presence of the most fuel rich region at the concave side of the neck contraction, indicating a fuel accumulation at that same region. This could be indicative of a recirculative phenomenon, which will be further investigated utilizing the particle image velocimetry (PIV).

3.2.2 Local Spectroscopy

Based on the preliminary image processing analysis three interest zones were established for the different flame morphologies, with an additional fourth zone for the Type II flame at the interior flame structure coupled to the central air slit. For each region, five acquisition points were established traversing the flame front with steps of 0.25 mm. These are displayed in the images coupled with a positioning grid, adjacently, the complete local equivalence ratio (ϕ) results for each flame type are represented with horizontal positioning adimensionalized by slot width ”w”.

Let us start by analyzing the exterior flame front of the Type II flame, as can be seen in Figure 3.14, there is a general tendency for a ϕ increase between equivalent positions for the three different heights except for outermost position, where position ”C” presents a lower ϕ value, which is not deemed as representative due to the close proximity of all the values and the previously discussed radical measurement uncertainty.

Continuing with the outside flame front, the ϕ value can be seen to obtain a maximum value for each measurement height, close to the location of strongest light emission, and progressively decrease

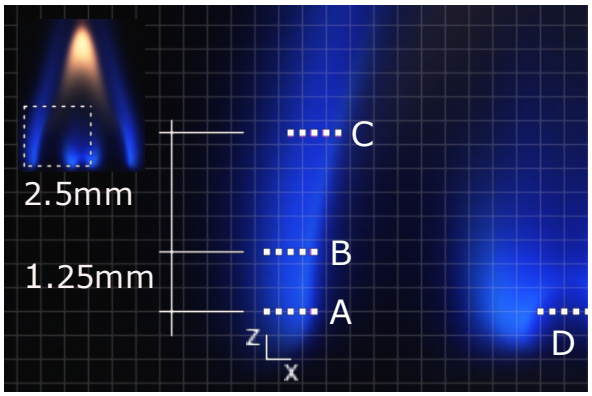

(a) Spectroscopy acquisition positioning detailed view

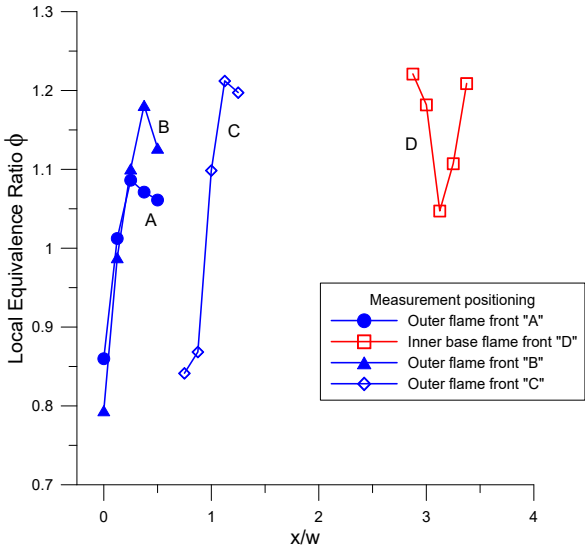

(b) Combined measurements.

Figure 3.14: Type II ($\phi_g = 3.2$) spectroscopy results.

towards the fuel-rich interior. This diminishing fuel presence at the flame front is connected to the existence of an interior yellow soot-producing region downstream, due to the excess unburnt fuel from both channels meeting at the flame top, as previously mentioned in the analysis of the image processing results from Figure 3.11.

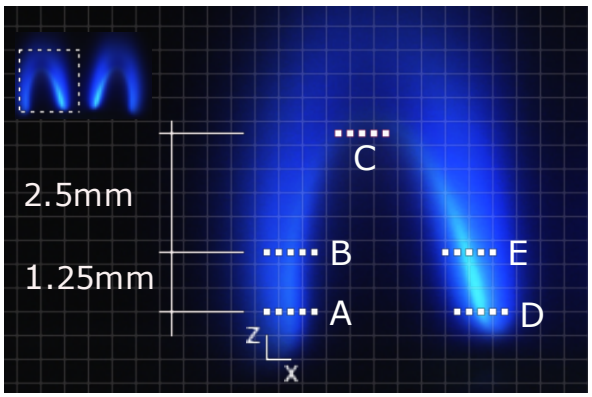

(a) Spectroscopy acquisition positioning detailed view

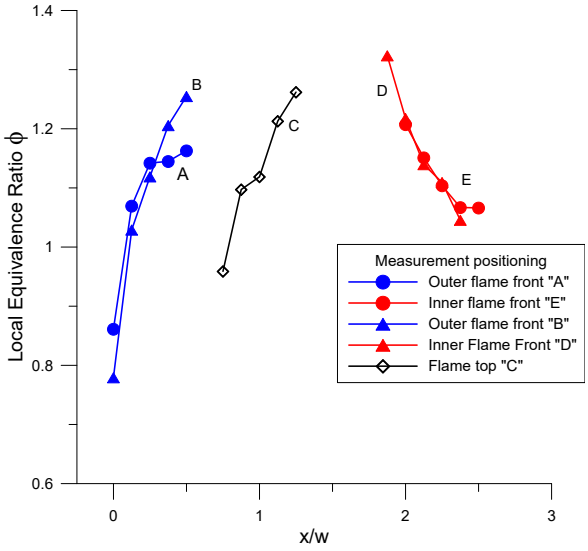

(b) Combined measurements

Figure 3.15: Type III ($\phi_g = 1$) spectroscopy results.

Regarding the results obtained for the type III flame, for the same measurement height and corresponding positions, the interior flame (depicted on the right-hand side in Figure 3.15(b), positions ”E” and ”D”) presents a higher local ϕ value, indicative of an increased fuel concentration towards the interior flame front, as expected due to the velocity gradient induced by the air jet.

Comparing the values obtained for the most interior positions corresponding to either side of the flame, it is observed that the difference between both is not as pronounced as the one observed in the

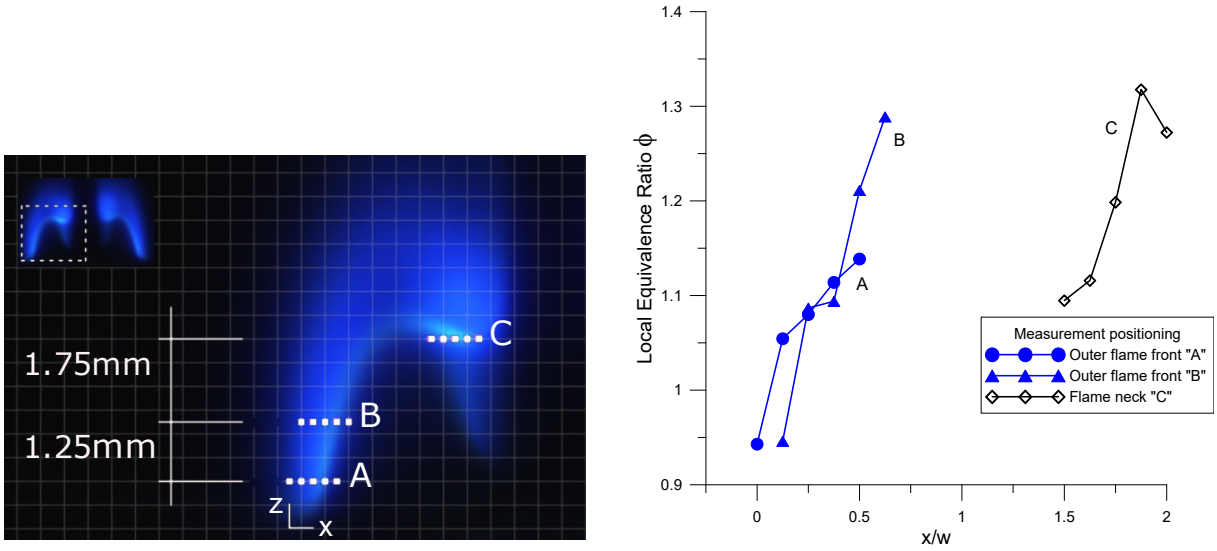

(a) Spectroscopy acquisition positioning detailed view

(b) Combined measurements

Figure 3.16: Type IV ($\phi_g = 0.3$) spectroscopy results.

preliminary numerical approach, nonetheless the same tendency is preserved.

Analyzing the exterior flame front (left-hand side) individually, for the three first measurements there is a ϕ decrease between both heights, showing that closer to the base, there is a slightly more pronounced air presence, confirming the image processing results.

In regards to the flame top measurement, ”C”, there is a clear increase in fuel concentration towards the innermost measurement positions, this is in accordance to the general fuel movement towards the lower-pressure central slot air jet positioned at the right-hand side.

As for flame Type IV, there is once again a generalized tendency in ϕ increase for corresponding positions at different heights for the outside flame front, but with no ϕ value inversion for the most interior points as seen in Type III. This is indicative of the existence of a mechanism impeding the free impingement of the fuel flow towards the central air jet, which would expectantly be greater due to a more intense velocity gradient for this last case ($V_r = 60$). The indication of such phenomenon could already be observed in the image processing results, through the presence of a rich zone in the curvature at the neck attachment.

Analyzing the neck attachment zone, the increased fuel presence ascertained from the image processing results is confirmed, there is a point of maximum ϕ located in this zone, pointing towards the possible existence of a fuel recirculation, defining this as an interest zone for the PIV analysis.

Combined Results

Combining the measurements obtained for the two shared exterior flame front locations (positions ”A” and ”B”) for the three flames under analysis, it is possible to ascertain the particular local differences in equivalence ratios between them. Figure 3.17(a) presents these results for the first measurement height and Figure 3.17(b) for the second one.

Observing the comparative measurements, the general range of local ϕ for the exterior flame front

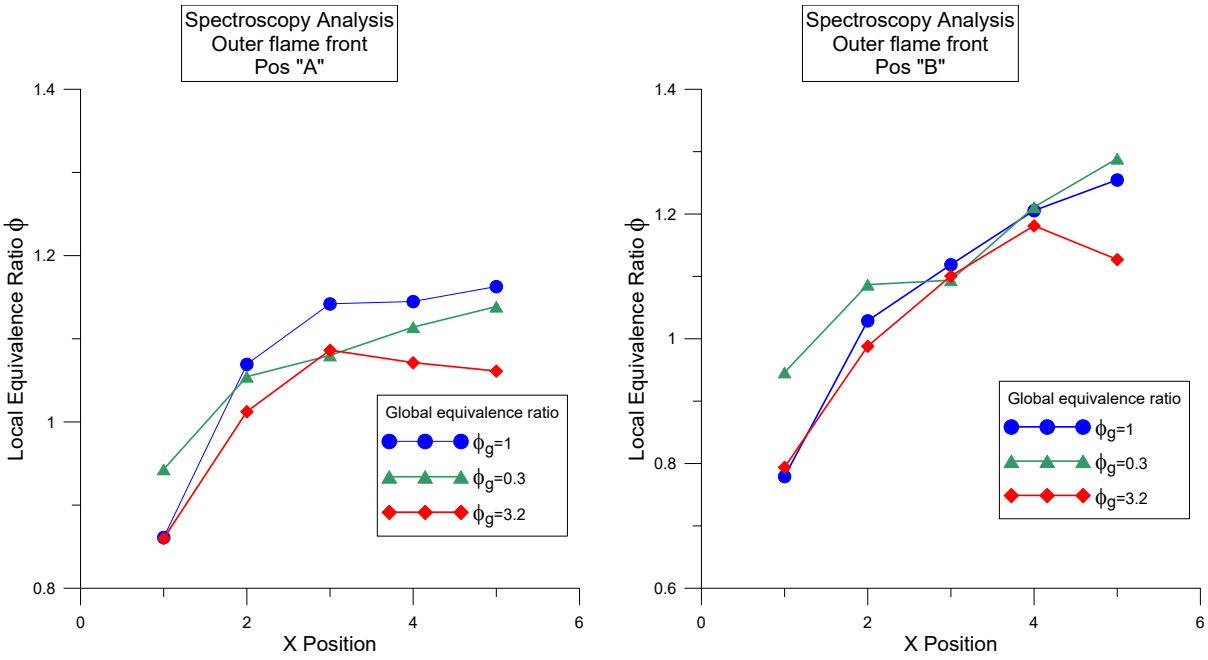

(a) Combined position A

(b) Combined position B

Figure 3.17: Combined exterior flame front spectroscopy measurements.

value is seen to be restricted between 0.7 and 1.3 and the behaviors for the two globally leaner flames ($\phi_g = 1$ and $\phi_g = 0.3$) are quite similar. The decreasing ϕ tendency of the globally richer flame ($\phi_g = 3.2$) evident in Figures 3.17 is not accentuated enough to

From the obtained results the notion of global equivalence ratio (ϕ_g) is once again verified to be purely indicative of a global reference value, and non-representative for the actual local values present in the IDF.

3.3 PIV Analysis

As an initial approach to the PIV analysis, it was important to establish the adequate parameters for the flow characterization, as previously mentioned in the technique methodology. Particularly the time between pulses (Δt), which has its effect at the time of the data acquisition, and the interrogation area (IA) dimension, which is a processing parameter.

For this purpose, the analysis is divided in three stages. Progressing from an initial isothermal (no flame) measurement for a single slit with the corresponding flow rate of the equivalent flame, allowing for a preliminary adjustment of the parameters with the theoretical velocity profile as a reference, followed by a second isothermal analysis stage with the three slit flow. Finally a third and final PIV study of the flames themselves with a complete vector mapping was performed, with a comparative analysis to the corresponding isothermal case and the flame velocity profile development downstream.

In terms of data measurement positioning, the common denomination ”base” is defined as 1 mm from the burner exit, and ”top(H)” was considered as a reference height from the type III flame This was utilized for the acquisition of all isothermal and comparative flame profiles, the downstream acquisitions

will be visually represented for each flame. Additionally, all the velocity profiles presented are measured in m/s and their positioning adimensionalized utilizing the slit width (w).

3.3.1 Isothermal Velocity Profile Analysis

Two different interrogation areas (IA) were considered for a 60 ms pulse interval in a single slit configuration. As evident in Figure 3.18, the 64x124 IA option shows a better defined profile with adequate symmetry. This was the profile utilized in the uncertainty analysis detailed in the previous chapter. Further developing the parameter analysis, two profile comparisons for a triple slit configuration are exhibited in Figures 3.19(a) and 3.19(b), it can observed that the triple slit velocity profile is not significantly affected by either of the two IA dimensions considered nor the two different pulse intervals.

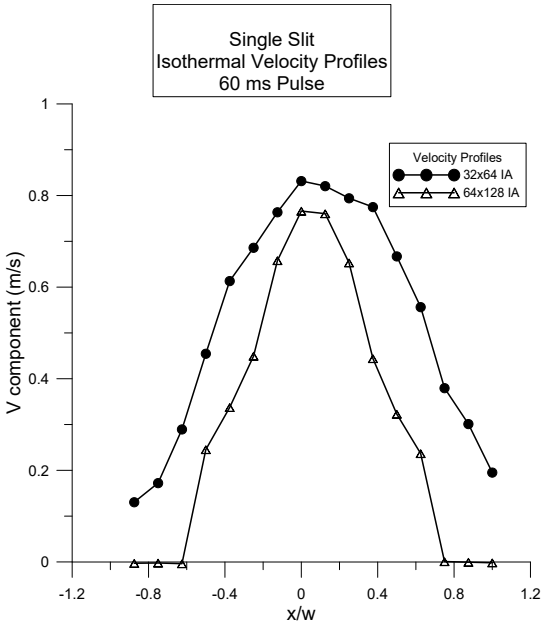

Figure 3.18: Single slit velocity measurements ; $\phi_g = 1$.

Concluding the preliminary isothermal analysis for this particular flame, both the single and triple slit configurations are compared for the same exact parameters (see Figure 3.20(a)) and for a fixed IA and a different pulse interval for each (see Figure 3.20(b). This was important to observe if there was a significant difference in the central slit velocities between the single and triple slot configurations. Due to the necessity of a pulse interval adjustment to account for the very significant velocity difference to the exterior slots. Reviewing the parameter influence detailed in the previous chapter, the relationship between the IA and the time interval, is highly velocity dependent, due to the possibility of a particle either completely leaving the IA before the second frame, or not being able to present any adequately detectable movement at all.

It can be observed that, for this case, there is a very good middle slit velocity correspondence between both configurations with a simultaneously adequate detection of both exterior slit flows, even if for the flame analysis, the velocities are comparably greater. A pulse interval value of 200 ms and IA dimension of 64x128 pixels were opted for the next stage.

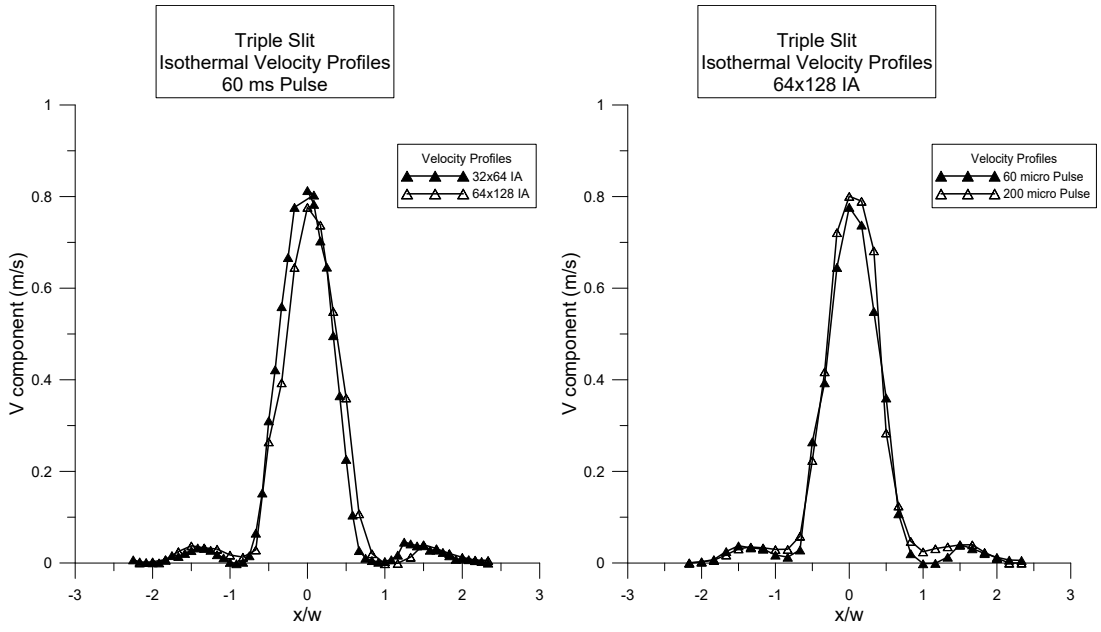

(a) Pulse $\Delta t = 60ms$. (b) IA 64x128.

Figure 3.19: Triple slit velocity measurements ; $\phi_g = 1$.

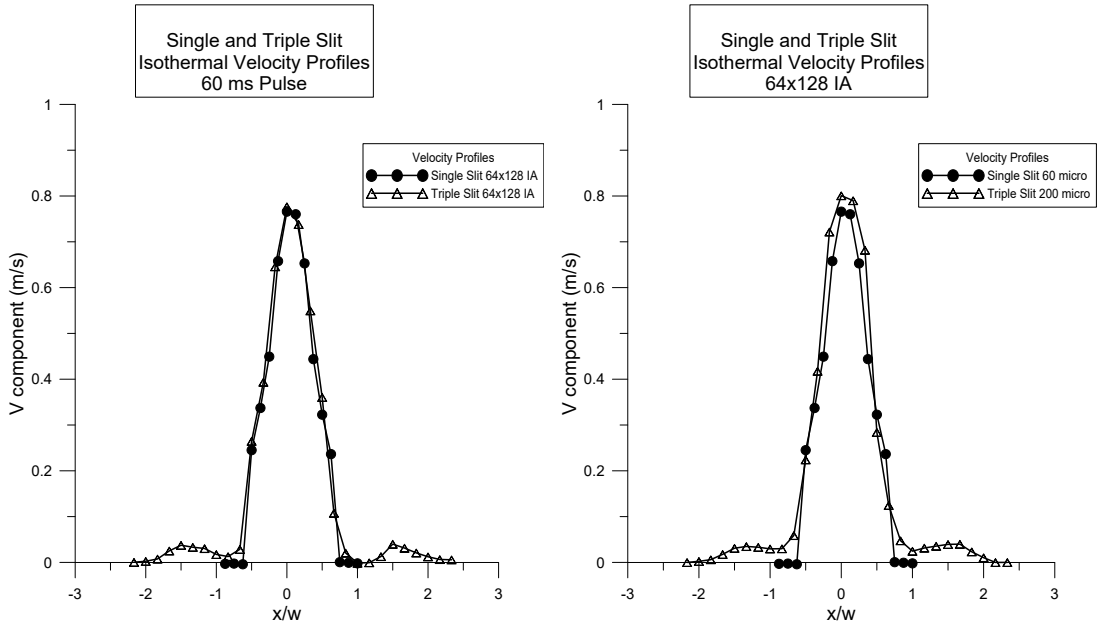

(a) Pulse $\Delta t = 60ms$; IA 64x128. (b) IA 64x128.

Figure 3.20: Triple and single slit velocity measurements ; $\phi_g = 1$.

Utilizing the insight into the parameter effects from the initial isothermal analysis, the analogous measurements of the velocity at the burner exit for the two other flame types under analysis, Type II ($\phi_g = 3.2$) and Type IV ($\phi_g = 0.3$) are presented in Figures 3.21(b) and 3.21(a) respectively. It is important to note that for the Type IV flame, where the velocity ratio between air and fuel is the highest ($V_r = 60$), there was the need to adopt two different IA dimensions for each channel in order to adequately detect the particle movements for both flow rates. A coarser dimensioning of 64x128 for

the central air slot, due to a higher velocity ($V_r = 60$) and predominantly vertically oriented flow, and a finer IA dimension of 32x32 for both fuel slots to properly detect the slower particle movement for the same fixed time interval and the now quite relevant horizontal flow movement due to the the fuel jet impingement towards the central air jet, approaching a cross-flow.

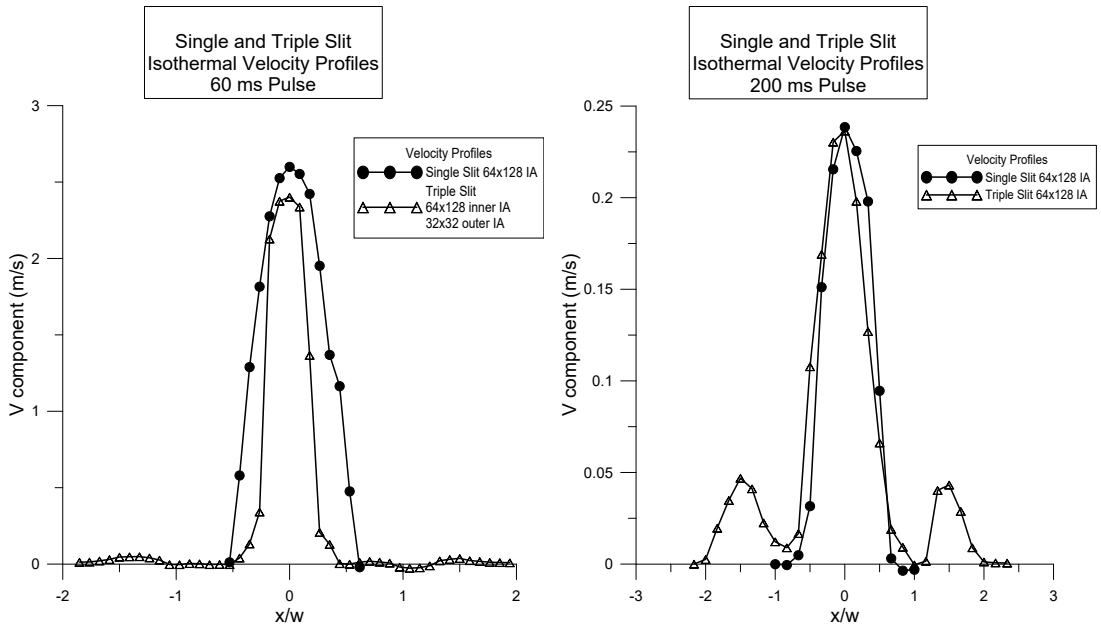

(a) Type IV ; $\phi_g = 0.3$. (b) Type II ; $\phi_g = 3.2$.

Figure 3.21: Triple slit velocity measurements.

3.3.2 Flame Velocity Profile Analysis

Type II

For the isothermal and flame comparison, two main observations are evident, firstly the central velocity increase at the base is much more substantial for the flame flow. This is due to the presence of the interior flame structure coupled to the central air slit at the base, completely enveloping the central flow. This generates low density hot combustion products that travel, downstream. Secondly, the points of maximum fuel velocity drift slightly outwards towards the exterior fuel slit edges, highlighted by the arrows in Figure 3.23(a).

This is explained by the the less intense velocity gradient experienced by the fuel particles towards the central air flow due to a smaller V_r in comparison to the previous flames and the presence of the initial flame front located outside of the fuel slit with a slight inwards tilt. The opposite effect can be detected in the Type IV flame velocity profiles depicted in Figure 3.28(a) by the two arrows, where a more intense velocity gradient caused by a value of $V_r = 60$ is reflected in an inward shifting of the maximum fuel velocity points.

Analyzing the velocity profile development downstream once again the momentum transfer between adjacent flows becomes evident with the formation of a parabolic profile, as observed for the previous flames, this acceleration tapers off towards the edges for the further downstream measurements.

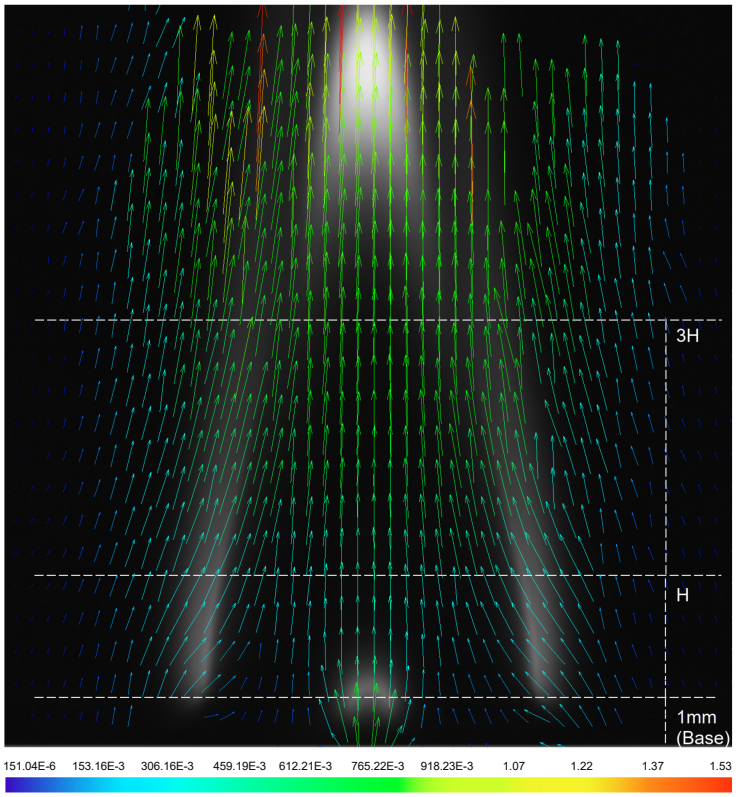

Figure 3.22: Type II vector mapping ($\Delta t = 200ms; \phi_g = 3.2$) ; H - defined from flame Type III height.

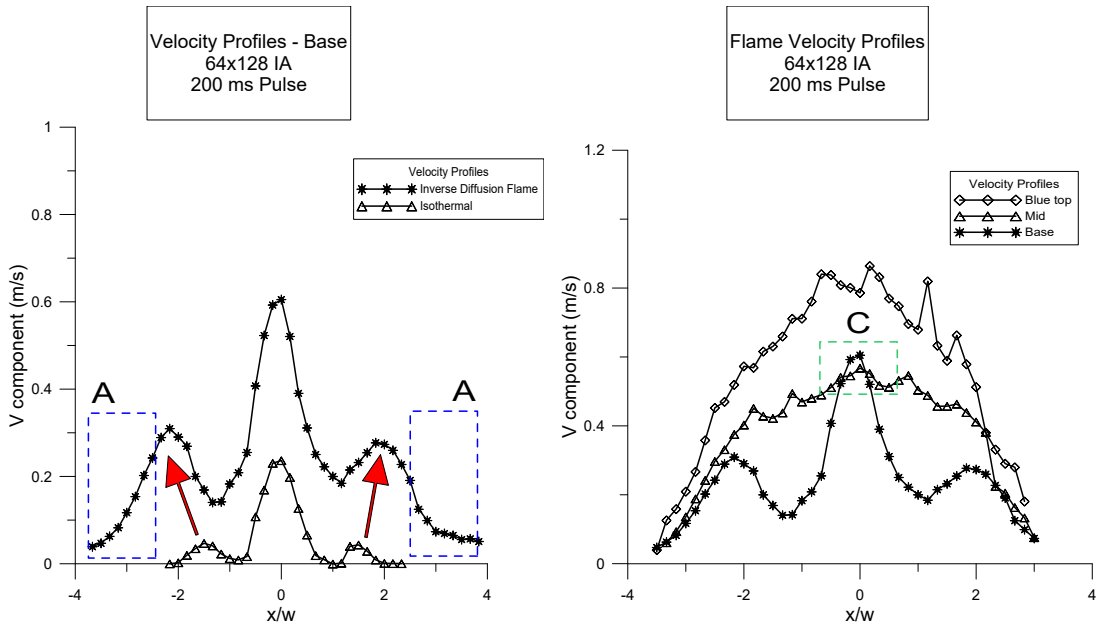

(a) Isothermal and Flame velocity profiles. Region "A" - entrainment particle movement.

(b) Profile development downstream. Region "C - velocity decrease zone.

Figure 3.23: Isothermal comparison and flame velocity profile development ; $\phi_g = 3.2$.

The main detail of interest is the velocity decrease between the flame base and mid measurements (delineated as region C), this is expected once again due to the presence of the smaller interior flame,

accelerating the particles through this small flame front, before traversing a non-reacting interior flame zone and meeting the upper flame front further downstream, re-accelerating during after-burning.

Type III

In terms of flame velocity profile analysis there are two main results of interest to consider, the velocity profile at the flame base in comparison to the same location for the isothermal case, as shown in Figure 3.25(a), and the velocity profile development of the flame itself, from the base to a height close to the flame top, as can be seen in Figure 3.25(b). To properly interpret these results, it is important to recall that the PIV isothermal cases utilized particle seeding exclusively in the burner slits and the flame cases used the addition of surrounding "ambient" particles with a much lower velocity vertical velocity component. These particles were utilized as a mean to evaluate the outside air entrainment.

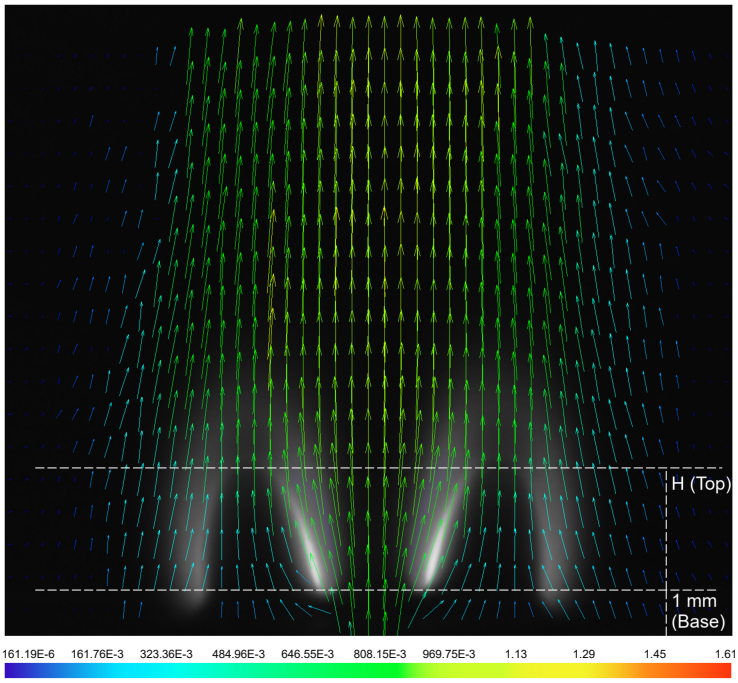

Figure 3.24: Type III vector mapping ($\Delta t = 200ms; \phi_g = 1$) ; H - defined as flame Type III height.

Let us first consider the isothermal and flame case comparison. As evident, for the same position there is a very substantial increase in particle velocity, in particular for the exterior slit (fuel) flows. Considering $\frac{V_{flame}}{V_{Iso}}$ as a local velocity ratio between the flame and isothermal case, the two main points of interest, the center line velocities of both the air and fuel slits, can be analyzed. For the central slit a value of $\frac{V_{flame}}{V_{Iso}} = 1.14$ is obtained, as for the fuel slits, averaging both sides, one obtains $\frac{V_{flame}}{V_{Iso}} = 11.06$. These velocity increments are caused by the hot gas expansion occurring at the flame front [53]. Even though the central air flow does not directly cross the flame front, it is surrounded by the two interior flame fronts, which can lead to heat transfer and consequently to a gas density decrease and particle acceleration.

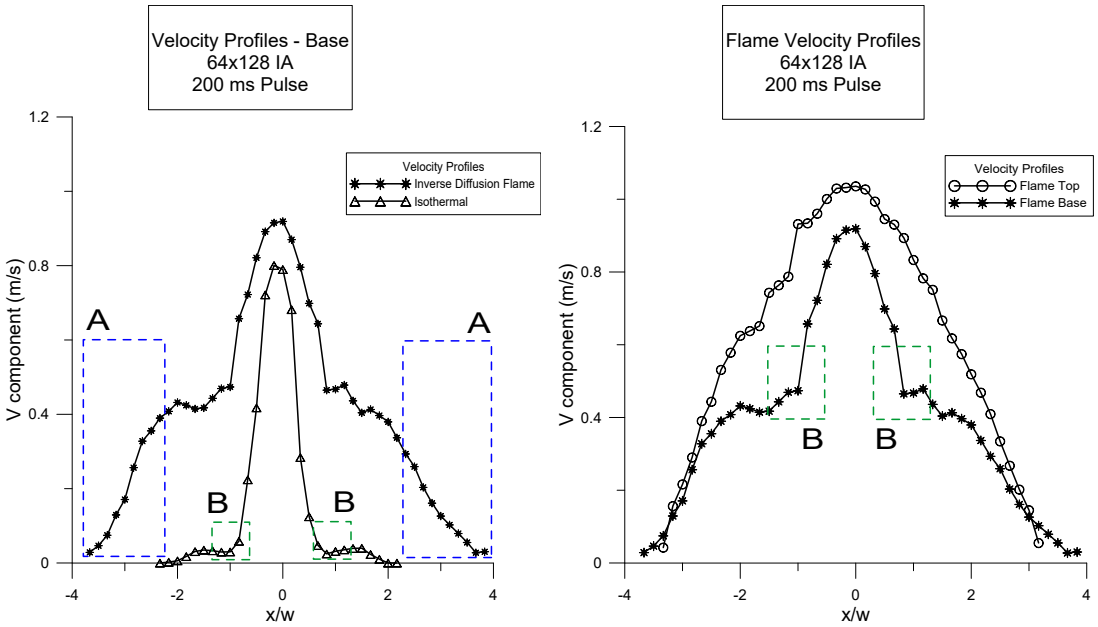

(a) Isothermal and Flame velocity profiles. Region "A" - (b) Profile development downstream. Region "B" - slot in-entrainment particle movement. Region "B" - slot interface terface velocity.
velocity.

Figure 3.25: Isothermal comparison and flame velocity profile development ; $\phi_g = 1$.

Another effect that can be clearly observed in this comparison is the outside air movement. There is a momentum increase in the otherwise stagnant air outside the fuel slits at the burner exit. This is caused by the pressure difference, shear forces and entrainment effect, effectively accelerating the outside particles, "pulling" them along the main flow lines (this effect is delineated as region "A" in Figure 3.25(a).

Analyzing the interface zone between air and fuel slits (delineated as zone "A"), another important detail can be observed. The velocity never reaches a null value between both slits, demonstrating the importance of the jet interactions and momentum transfer that start occurring upstream quite close to the burner exit.

Considering the velocity profile development in the flame case (see Figure 3.25(b)), the momentum transfer between fuel and air flows is clearly visible. The initial profile where an aggressive velocity gradient was identified between slits gives way to a much smoother parabolic developed profile. Besides this, the further increase in velocity as the particles traverse the flame front towards the top is visible. This effect tapers approaching the edges, due to the air entrainment being much stronger closer to the base of the flame, causing the small amount of entrainment particles that might still be affected at the flame top, to not have the opportunity to accelerate in the burning flame front. Considering again the the slit center line velocities, let us relate the values between both positions to obtain a relative increase. For the central air flow $\frac{V_{top}}{V_{base}} = 1.13$ and for an average of both fuel flows $\frac{V_{top}}{V_{base}} = 1.59$.

Type IV

Observing the vector map (Figure 3.26), the fuel flows are seen to start impinging the central air jet immediately after the burner exit (before the flame base). After this mixture and momentum exchange, there is an outwards movement as the particles cross the intensely reacting neck constrainment region. Bearing in mind the high fuel concentration previously detected in this region, using the numerical ϕ assessment algorithm and confirmed through the local spectroscopy, a further IA dimension refinement was applied to this region of interest. The laser pulse interval utilized in the previous analysis was maintained but the IA was reduced to 16x32 pixels in order to accurately measure the more intricate details of the particle movements in the region of interest, which can be lost when utilizing an inadequate IA sizing or pulse interval, as described in sub-section 2.2.3.

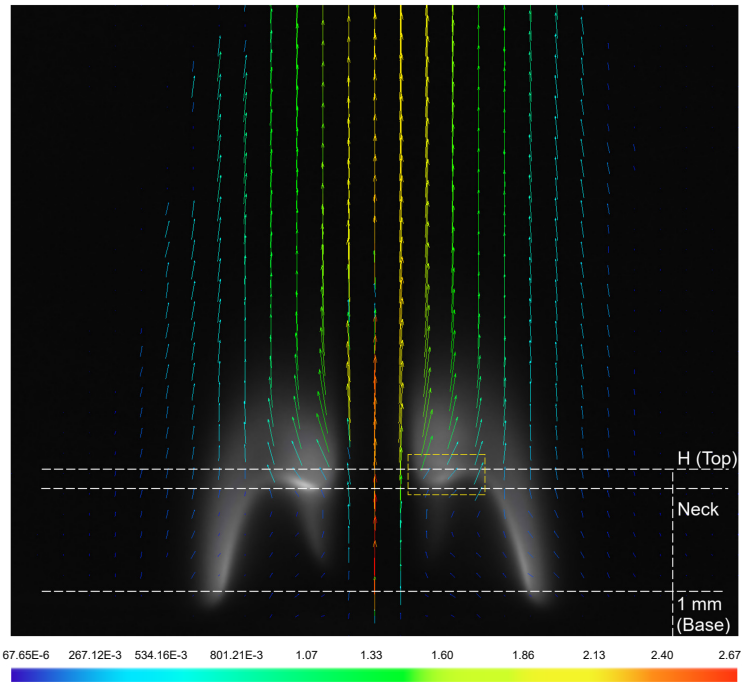

Figure 3.26: Type IV vector mapping ($\Delta t = 200ms; \phi_g = 0.3$). Detailed view location delineated by yellow dashed line ; H - defined as flame Type III height.

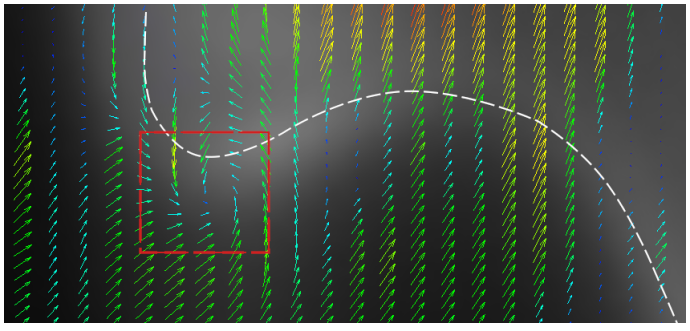

Figure 3.27: Type IV Neck vector mapping detailed view ($\Delta t = 200ms; IA = 16 \times 32px; \phi_g = 0.3$).

Figure 3.27 presents the region of interest with the flame front centerline delineated in dashed line as a visualization aid. The refined analysis detected a flow recirculation zone at the neck constrainment (red dashed highlight region). The neck region has been observed in a number of studies as previously mentioned, but a flow reversal and recirculation in this region has seldom been reported. Elbaz et al. [53] found neck flow reversal regions for singular very specific flow condition ($V_r = 20.7; Re_{air} = 2500$) in a co-annular (CoA) burner. This was associated with poor mixing as the fuel jets are deflected outwards and resulted in the generation of an outer yellow soot ring. For the present analysis, although the Reynolds number is inferior ($Re_{air} = 1185$), the velocity ratio is substantially greater ($V_r = 100$) and there is no apparent generation of a yellow soot-producing region. In fact, the flame is decreasing in height towards this regime, indicating an even more intense mixing happening in the air-fuel jet interfaces [18, 21, 53]. Therefore, the flow reversion phenomenon found by Elbaz et al. in the neck region does not seem to be correlated with the case under study.

Delving further into the analysis of this flow recirculation region, the work developed by Dong et al. [20] with a circumferential arranged ported (CAP) burner, found a much more prevalent range of IDFs with a neck constrainment region. As Re_{air} exceeded 300, the recirculation zone was seen to be present and this region was maintained up to flame blowoff. Therefore, the present findings show a much better correlation to the results of Dong et al. for the CAP burner, with the increasing V_r aggravating fuel jets impingement acting as cross-flows for the central air jet. The high pressure formed around the impingement stagnation point creates a recirculation zone, functioning as a structural stabilization aid mechanism at the flame neck. The stabilization effect of this impingement-induced recirculation zone is proved to be very effective in guaranteeing an extremely globally lean range of flame operating conditions.

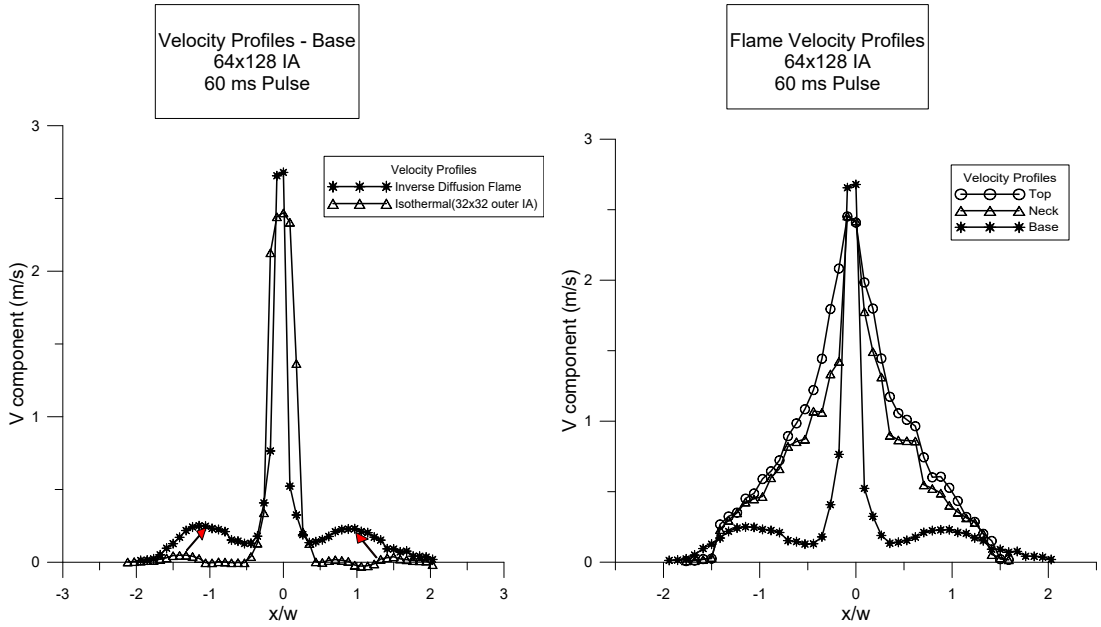

(a) Isothermal and Flame velocity profiles.

(b) Profile development downstream.

Figure 3.28: Isothermal comparison and flame velocity profile development ; $\phi_g = 0.3$.

In regards to the isothermal and flame velocity profile comparison, once again the velocity increase is evident, in particular for the outer fuel flows as well as the outside air entrainment. For the velocity profile development, a main detail can be observed for this flame morphology. In contrast to the velocity increase for the outer flows, due to the presence of the flame front, the central air jet velocity diminishes downstream along the central line. This is to be expected due to the structure of the flame ”neck”. Some of the air will progress downstream without participating in the flame front combustion, thus naturally shedding velocity by momentum transfer to the surroundings. This results in the highest air slit center line velocity being measured at the burner exit, and the lowest at the flame top (as can be seen in Figure 3.28(b)).

It is relevant to note that for the Type III flame, the central air vertical pathway was also clear of any flame region. However, Type IV does not possess the two interior flame fronts adjacent to the air jet increasing the central jet velocity due to the momentum transfer from the hot accelerated combustion products exiting in normal direction from the flame front and the pre-heating effect caused by flame heat conduction and radiation.

3.4 Morphological analysis overview

In summary, each of the three techniques, utilized with the goal of characterizing the IDF multi-slot burner morphologies, provided an important input in understanding the working mechanisms of the flames. The fuel and air flow interactions visualized with the particle image velocimetry together with the measurements of local equivalence ratio (ϕ) values provided a fundamental view into how the various flame structures, observed initially through the flame photography, react to the alterations in velocity ratio (V_r). To further illustrate the mechanisms characteristic to each flame type, a condensed flame schematic is presented in Figure 3.29 for each of the three flame types (and respective global equivalence ratio (ϕ_g) ranges), II, III and IV studied in depth experimentally.

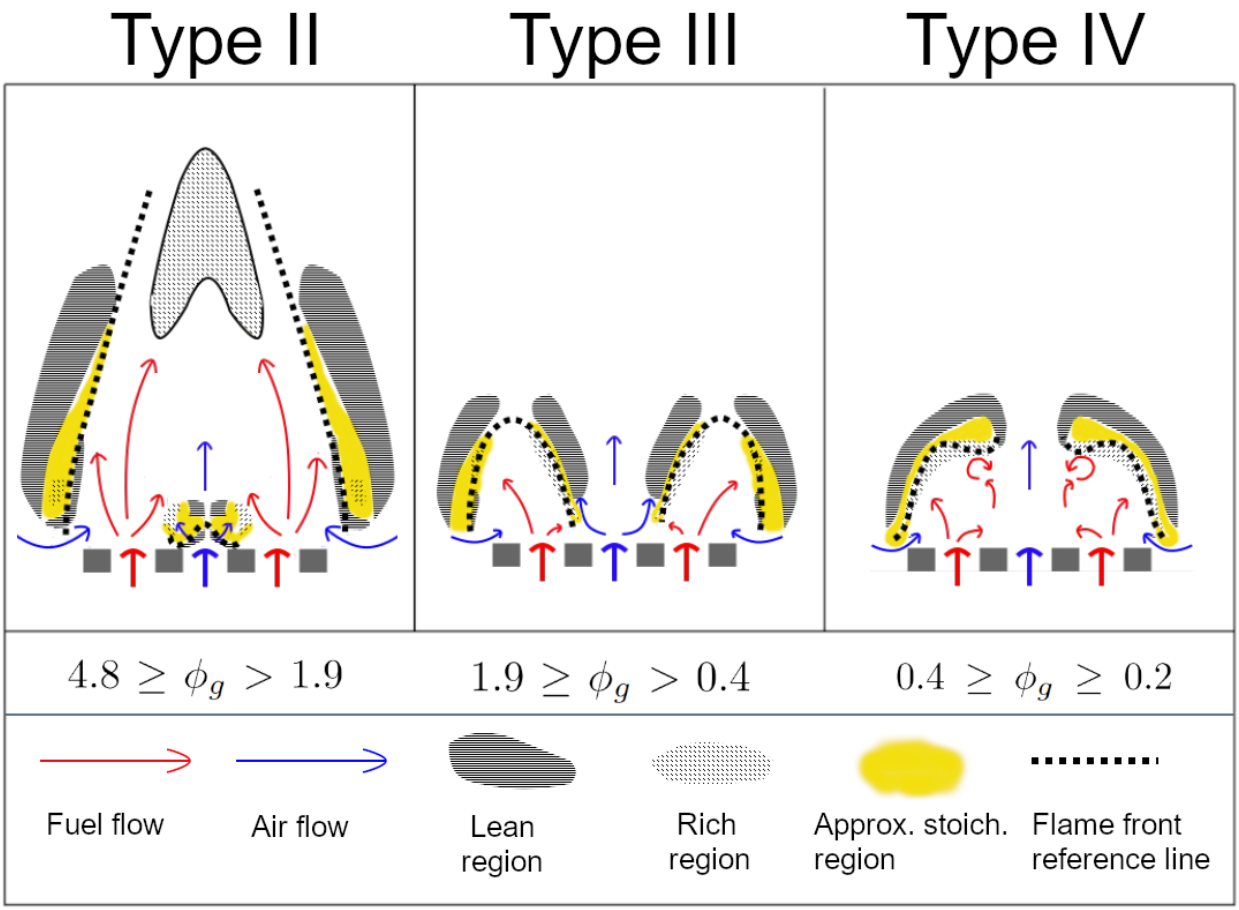

Figure 3.29: Condensed flame type schematic.

Chapter 4

Conclusions

4.1 Present work contributions

The main goal of this work was to characterize the morphology of methane inverse diffusion flames in a multi-slot burner. To achieve this, the first step was to obtain a working range of stable flames with characteristic parameters. In accordance to the previous research on this topic, the air flow rate was taken as the main variable, defining the two fundamental parameters, the global equivalence ratio (ϕ_g) and the velocity ratio (V_r). This working range was obtained for two distinct flame powers of 238 W and 476 W, through the control of the fuel flow rate. From the obtained flames, three main characteristic morphologies were identified as flame types and used for the consequent analysis techniques.

All flames types were subject to a chemiluminescence study, both utilizing an image processing algorithm and optical spectroscopy measurements. The obtained local equivalence ratios were analyzed in detail individually and comparatively for the exterior flame front positions. With the goal of understanding the underlying mechanisms associated with the different flame structures a particle image velocimetry (PIV) technique was utilized. This allowed the construction of the velocity vector maps of each flame type, including the outside particle movement and visualization of air entrainment. On top of the vector maps, a number of velocity measurements were made at different flame heights and at their flowrate-equivalent isothermal cases. This permitted a comparison between the isothermal and flame cases and for a study of the evolution of the velocity profile along the flames.

A summary of the most important findings of this thesis is itemized below:

1. Four distinct methane IDF flame types for the complete working range of the multi-slot burner were identified: Type I characterized by the triangular shape of the flame front with a clear yellow soot production zone; Type II presenting a transition structure, where an inner flame front is generated but a disconnect is maintained with the outside flame fronts; Type III characterized by the continuous symmetric flame fronts separated by the air jet and the absence of any yellow soot producing zone, and finally Type IV, where the interior flame fronts rise and stabilize in a ”neck-like” structure with a completely blue flame and no visible soot production.

2. It was verified that the lean blowout limit is not affected by the fuel flow rate, as previously shown

by Zhang et al. for a CoA burner [54].

3. The velocity ratio (V_r) was found to be an important governing parameter in the definition of the flame structures, This is due to its role in the air-fuel jet entrainment. The shear forces and pressure gradients generated between jets, through the V_r increase, intensify the inter-jet mixing, increasing the local reaction rates and shortening the visual flame height.

4. The formation of the neck-like structure was found to occur at $Re_{air} = 355$ for the 238 W flame and $Re_{air} = 450$ for the 476 W one, which are in agreement with the results for CAP burners [21].

5. The sudden visual flame height reduction occurring at the transition to flame Type III was detected at $V_r = 10$ which compared to the previously reported value of $V_r = 15$ at the moment of a substantial height reduction for CoA burner [53], shows a quite good accordance.

6. An equivalence ratio calibration equation based on the combination of the OH^*/CH^*,C_2^*/CH^* and C_2^*/OH^* radical emission ratios of a premixed methane flame for the same burner was established. Presenting a wide ϕ range sensitivity.

7. Through the measurement of the local equivalence ratio (ϕ), it was possible to detect a clear contrast between the interior and exterior flame fronts for flame Type III. Presenting a more significant fuel presence towards the interior flame front, which is indicative of the fuel flow movement towards the high velocity air jet. A similar movement of fuel was detected for Type II, with the formation of a richer zone at the smaller central flame front.

8. For flame Type IV, through the chemiluminescence spectroscopy, a rich area was detected at the neck constrainment region, indicating a possible recirculation phenomenon. This was verified through the velocity vector mapping obtained with the particle image velocimetry (PIV) technique. The high pressure formed around the impingement stagnation point creates a recirculation zone, functioning as a structural stabilization aid mechanism at the flame neck. The stabilization effect of this impingement-induced recirculation zone is proved to be very effective in guaranteeing an extremely globally lean range of flame operating conditions.

4.2 Future work guidelines

The work developed on this thesis was the onset of the research into inverse diffusion flames in IN+, from the knowledge obtained through this study, a preliminary methodological framework can be established to further this research. Guided by the modern investigative efforts into leaner combustion solutions and more effective pollutant emission control, a number of steps are suggested to gain additional insights into the applicability of these promising IDFs.

1. A gas emission analysis would be quite important in aiding the understanding of the combustion characteristics of each flame type. In particular the emissions of NO_x and CO, and their variation across the IDF range in correlation to the global equivalence ratio (ϕ_g) and the velocity ratio (V_r)

2. Flame temperature measurements would also be a useful approach for an even more complete characterization of these particular IDFs. Allowing for a better understand of the heat transfer mechanisms in these particular flames.

3. In terms of fuel there are two pathways of particular interest where the methane IDF study can be further developed, in particular for these multi-slot burners. The enrichment with other species with unique thermophysical properties such as H_2, can prove fruitful in extending even further the lean working range and mitigate the CO emissions associated with the temperature decrease; Additionally, it would be of interest to study the IDF behaviour under different biogas compositions utilizing CH_4, CO_2 and eventually the combination with H_2 enrichment.

4. Regarding the burner geometry, it is important to understand the effects of the burner length, slot width and length in the structural disposition of these IDFs. The study of these geometric characteristics and how they could eventually alter the flame structures and inter-jet mixing phenomena is important to determine the most efficient way of reaching the less-polluting lean regimes and realizing the potential of the IDF.

Bibliography

[1] F. Vivas, A. D. las Heras, F. Segura, and J. Andújar. A review of energy management strategies for renewable hybrid energy systems with hydrogen backup. *Renewable and Sustainable Energy Reviews*, 82:126–155, feb 2018.

[2] J. N. Friend. *The Chemistry of Combustion*. Gurney & Jackson, 1922.

[3] S. P. Burke and T. E. W. Schumann. Diffusion flames. *Industrial & Engineering Chemistry*, 20(10): 998–1004, oct 1928.

[4] J. Arthur and D. Napier. Formation of carbon and related materials in diffusion flames. *Symposium (International) on Combustion*, 5(1):303–316, jan 1955.

[5] K.-T. Wu and R. H. Essenhigh. Mapping and structure of inverse diffusion flames of methane. *Symposium (International) on Combustion*, 20(1):1925–1932, jan 1985.

[6] D. B. Makel and I. M. Kennedy. Soot formation in laminar inverse diffusion flames. *Combustion Science and Technology*, 97(4-6):303–314, may 1994.

[7] J. Du. The effect of flame structure on soot-particle inception in diffusion flames,. *Combustion and Flame*, 100(3):367–375, feb 1995.

[8] C. R. Shaddix, T. C. Williams, L. G. Blevins, and R. W. Schefer. Flame structure of steady and pulsed sooting inverse jet diffusion flames. *Proceedings of the Combustion Institute*, 30(1):1501–1508, jan 2005.

[9] M. A. Mikofski, T. C. Williams, C. R. Shaddix, and L. G. Blevins. Flame height measurement of laminar inverse diffusion flames. *Combustion and Flame*, 146(1):63 – 72, 2006. ISSN 0010-2180.

[10] M. Mikofski, T. Williams, C. Shaddix, A. Fernandezpello, and L. Blevins. Structure of laminar sooting inverse diffusion flames. *Combustion and Flame*, 149(4):463–478, jun 2007.

[11] F. Roper, C. Smith, and A. Cunningham. The prediction of laminar jet diffusion flame sizes: Part II. experimental verification. *Combustion and Flame*, 29:227–234, jan 1977.

[12] J. Miao, C. Leung, C. Cheung, and R. Leung. Flame stability and structure of liquefied petroleum gas-fired inverse diffusion flame with hydrogen enrichment. *Word Acad Sci*, pages 720–725, 01 2012.

[13] L. Sze, C. Cheung, and C. Leung. Temperature distribution and heat transfer characteristics of an inverse diffusion flame with circumferentially arranged fuel ports. *International Journal of Heat and Mass Transfer*, 47(14-16):3119–3129, jul 2004.

[14] L. Sze, C. Cheung, and C. Leung. Appearance, temperature, and NOx emission of two inverse diffusion flames with different port design. *Combustion and Flame*, 144(1-2):237–248, jan 2006.

[15] A. Sobiesiak and J. C. Wenzell. Characteristics and structure of inverse flames of natural gas. *Proceedings of the Combustion Institute*, 30(1):743–749, jan 2005.

[16] A. Elbaz and W. Roberts. Flame structure of methane inverse diffusion flame. *Experimental Thermal and Fluid Science*, 56:23–32, jul 2014.

[17] H. Zhen, Y. Choy, C. Leung, and C. Cheung. Effects of nozzle length on flame and emission behaviors of multi-fuel-jet inverse diffusion flame burner. *Applied Energy*, 88(9):2917–2924, sep 2011.

[18] L. Dong, C. Cheung, and C. Leung. Combustion optimization of a port-array inverse diffusion flame jet. *Energy*, 36(5):2834 – 2846, 2011. ISSN 0360-5442.

[19] S. Chander and A. Ray. Flame impingement heat transfer: A review. *Energy Conversion and Management*, 46(18-19):2803–2837, nov 2005.

[20] L. Dong, C. Cheung, and C. Leung. Heat transfer characteristics of an impinging inverse diffusion flame jet – part i: Free flame structure. *International Journal of Heat and Mass Transfer*, 50(25-26): 5108–5123, dec 2007.

[21] L. Dong, C. Cheung, and C. Leung. Heat transfer characteristics of an impinging inverse diffusion flame jet. part II: Impinging flame structure and impingement heat transfer. *International Journal of Heat and Mass Transfer*, 50(25-26):5124–5138, dec 2007.

[22] A. Kotb and H. Saad. A comparison of the thermal and emission characteristics of co and counter swirl inverse diffusion flames. *International Journal of Thermal Sciences*, 109:362–373, nov 2016.

[23] H. Zhen, C. Cheung, C. Leung, and H. Li. Thermal and heat transfer behaviors of an inverse diffusion flame with induced swirl. *Fuel*, 103:212–219, jan 2013.

[24] H. Zhen, C. Leung, and C. Cheung. Heat transfer from a turbulent swirling inverse diffusion flame to a flat surface. *International Journal of Heat and Mass Transfer*, 52(11-12):2740–2748, may 2009.

[25] H. Zhen, C. Leung, and C. Cheung. Thermal and emission characteristics of a turbulent swirling inverse diffusion flame. *International Journal of Heat and Mass Transfer*, 53(5-6):902–909, feb 2010.

[26] W. Partridge. Nitric oxide formation by inverse diffusion flames in staged-air burners. *Fuel*, 74(10): 1424–1430, oct 1995.

[27] S. Mahesh and D. Mishra. Flame stability and emission characteristics of turbulent LPG IDF in a backstep burner. *Fuel*, 87(12):2614–2619, sep 2008.

[28] F. Escudero, A. Fuentes, R. Demarco, J.-L. Consalvi, F. Liu, J. Elicer-Cortés, and C. Fernandez-Pello. Effects of oxygen index on soot production and temperature in an ethylene inverse diffusion flame. *Experimental Thermal and Fluid Science*, 73:101–108, may 2016.

[29] J. Miao, C. Leung, C. Cheung, Z. Huang, and H. Zhen. Effect of hydrogen addition on overall pollutant emissions of inverse diffusion flame. *Energy*, 104:284 – 294, 2016. ISSN 0360-5442.

[30] M. Abdelaal, S. Ali, A. Radwan, and A. Ismail. INVESTIGATION OF a NEW DESIGN OF INVERSE DIFFUSION FLAME BURNER. *Journal of Al-Azhar University Engineering Sector*, 11(41):1299–1309, oct 2016.

[31] S. R. Turns. *An Introduction to Combustion: Concepts and Applications*. McGraw-Hill Education, 2011. ISBN 9780073380193.

[32] V. de Brederode. *Aerodinâmica Incompressível : Fundamentos*. IST Press, 2018.

[33] F. M. White. *Fluid Mechanics*. McGraw-Hill Education - Europe, 2015. ISBN 0073398276.

[34] D. P. Mishra. *Experimental Combustion: An Introduction*. CRC Press, 2017. ISBN 9781138074217.

[35] S. Mahesh and D. Mishra. Flame structure of LPG-air inverse diffusion flame in a backstep burner. *Fuel*, 89(8):2145–2148, aug 2010.

[36] A. G. Gaydon. Flame spectrophotometry. In *The Spectroscopy of Flames*, pages 320–337. Springer Netherlands, 1974.

[37] T. Trindade, A. Ferreira, and E. Fernandes. Characterization of combustion chemiluminescence: An image processing approach. *Procedia Technology*, 17:194–201, 2014.

[38] J. Kojima, Y. Ikeda, and T. Nakajima. Spatially resolved measurement of oh*, ch*, and c2* chemiluminescence in the reaction zone of laminar methane/air premixed flames. *Proceedings of the Combustion Institute*, 28(2):1757–1764, jan 2000.

[39] Y. Hardalupas and M. Orain. Local measurements of the time-dependent heat release rate and equivalence ratio using chemiluminescent emission from a flame. *Combustion and Flame*, 139(3): 188–207, nov 2004.

[40] M. G. De Giorgi, A. Sciolti, S. Campilongo, and A. Ficarella. Flame structure and chemiluminescence emissions of inverse diffusion flames under sinusoidally driven plasma discharges. *Energies*, 10(3), 2017. ISSN 1996-1073.

[41] B. Higgins, M. McQuay, F. Lacas, J. Rolon, N. Darabiha, and S. Candel. Systematic measurements of oh chemiluminescence for fuel-lean, high-pressure, premixed, laminar flames. *Fuel*, 80(1):67 – 74, 2001. ISSN 0016-2361.

[42] R. Bastiaans. Cross-correlation piv : theory, implementation and accuracy. *Compustion Technology*, 4, 01 2000.

[43] K. Okamoto, S. Nishio, T. Saga, and T. Kobayashi. Standard images for particle-image velocimetry. *Measurement Science and Technology*, 11(6):685–691, may 2000.

[44] M. Raffel, C. Willert, and J. Kompenhans. *Particle Image Velocimetry: A Practical Guide*. 1998.

[45] A. Melling. Tracer particles and seeding for particle image velocimetry. *Measurement Science and Technology*, 8:1406, 01 1999.

[46] C. Brossard, J.-C. Monnier, P. BARRICAU, F. Vandernoot, Y. Le Sant, F. Champagnat, and G. Le Besnerais. Principles and applications of particle image velocimetry. 1, 2009.

[47] B. A. Rabee. The effect of inverse diffusion flame burner-diameter on flame characteristics and emissions. *Energy*, 160:1201 – 1207, 2018. ISSN 0360-5442.

[48] K. Ha and S. Choi. Cross-sectional characteristics of visible emission spectra in partially premixed flames. *International Communications in Heat and Mass Transfer*, 26(8):1139–1149, nov 1999.

[49] A. Hamins, J. Yang, and T. Kashiwagi. An experimental investigation of the pulsation frequency of flames. *Symposium (International) on Combustion*, 24(1):1695–1702, jan 1992.

[50] R. F. Huang, J.-T. Yang, and P.-C. Lee. Flame and flow characteristics of double concentric jets. *Combustion and Flame*, 108(1-2):9–23, jan 1997.

[51] I. Kimura. Stability of laminar-jet flames. *Symposium (International) on Combustion*, 10(1):1295–1300, jan 1965.

[52] G. Sidebotham and I. Glassman. Flame temperature, fuel structure, and fuel concentration effects on soot formation in inverse diffusion flames. *Combustion and Flame*, 90(3-4):269–283, sep 1992.

[53] A. M. Elbaz and W. L. Roberts. Experimental characterization of methane inverse diffusion flame. *Combustion Science and Technology*, 186(9):1249–1272, 2014.

[54] Y. Zhang and P. B. Sunderland. Quenching limits of inverse diffusion flames with enriched oxygen. *Combustion and Flame*, 162(6):2743–2745, jun 2015.

[55] T. Takeno and Y. Kotani. An experimental study on the stability of jet diffusion flame. *Acta Astronautica*, 2(11-12):999–1008, nov 1975.

[56] L. Vanquickenborne and A. van Tiggelen. The stabilization mechanism of lifted diffusion flames. *Combustion and Flame*, 10(1):59–69, mar 1966.

[57] R. M. L. H. Araújo. Study of a non-intrusive technique, based on ccd cameras, to estimate the fuel-air ratio in flames. Master's thesis, Instituto Superior Técnico, June 2019.

Appendix A

Burner channel technical drawings

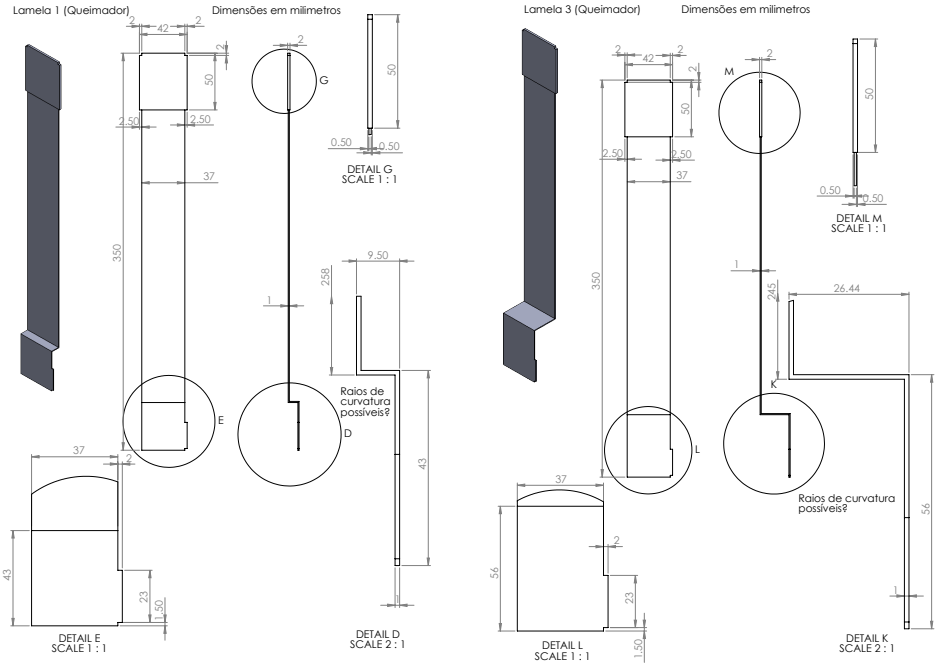

(a) Interior burner channel plate 1.

(b) Interior burner channel plate2.

Figure A.1: Interior burner plate technical drawings. (Dimensions in millimeters)

A.1 General relative error table

	Relative error[%]				
	e_{Q_A}	e_{Q_F}	e_ϕ	e_{U_A}	e_{U_F}
$\phi_g = 152.3$	8.80	1.65	18.79	9.59	0.36
$\phi_g = 76.2$	4.80	1.65	11.64	5.59	0.36
$\phi_g = 38.1$	2.80	1.65	8.65	3.59	0.36
$\phi_g = 19.0$	1.80	1.65	7.51	2.59	0.36
$\phi_g = 9.5$	1.30	1.65	7.09	2.09	0.36
$\phi_g = 4.8$	1.05	1.65	5.19	2.45	0.36
$\phi_g = 3.2$	1.63	1.65	4.91	1.89	0.36
$\phi_g = 2.4$	1.43	1.65	4.49	1.62	0.36
$\phi_g = 1.9$	1.30	1.65	4.26	1.46	0.36
$\phi_g = 1.6$	1.22	1.65	4.69	1.48	0.36
$\phi_g = 1.2$	1.11	1.65	4.14	1.26	0.36
$\phi_g = 1.0$	1.06	1.65	5.47	2.32	0.36
$\phi_g = 0.6$	1.47	1.65	5.42	1.87	0.36
$\phi_g = 0.4$	1.24	1.65	4.70	1.39	0.36
$\phi_g = 0.3$	1.05	1.65	5.77	1.67	0.36

Table A.1: Associated relative error values.

Appendix B

Additional isothermal velocity analysis

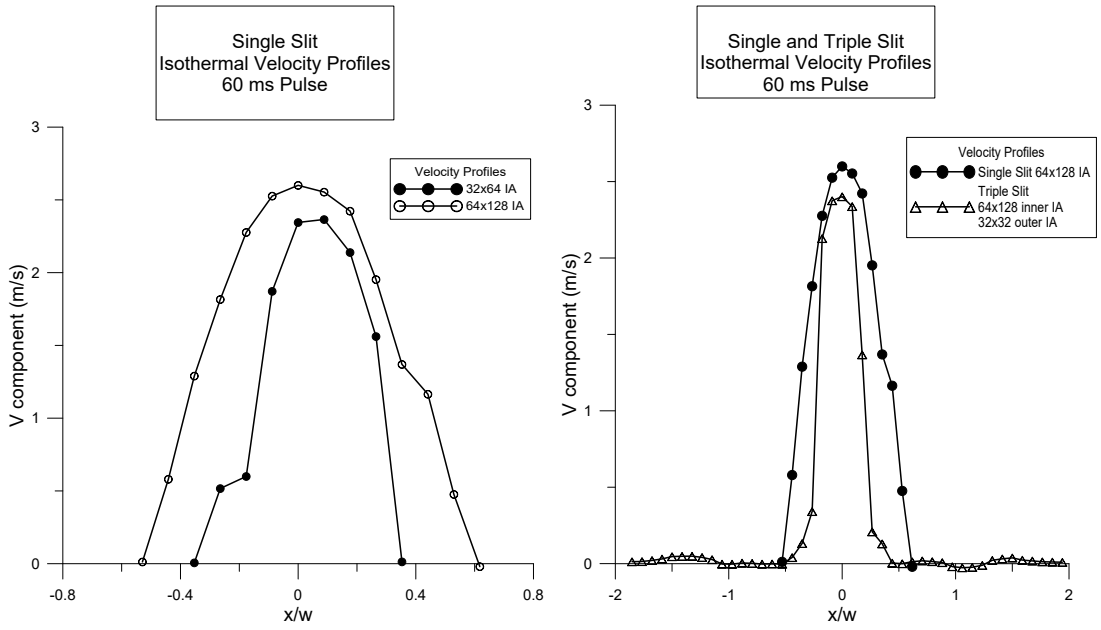

(a) Single slit velocity measurements ; $\phi_g = 0.3$. (b) Triple and single slit velocity measurements ; $\phi_g = 0.3$.

Figure B.1: Single and triple slit isothermal analysis ; $\phi_g = 0.3$.

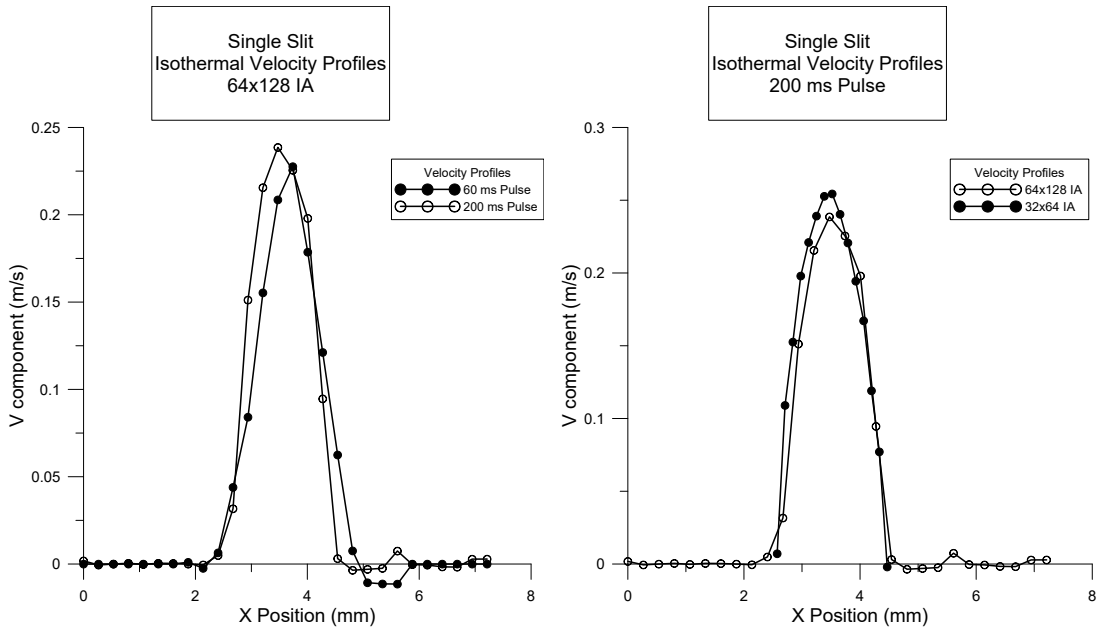

(a) Single slit velocity measurements ; $\phi_g = 3.2$; IA 64x128

(b) Triple and single slit velocity measurements ; $\phi_g = 3.2$; $\delta t = 200ms$

Figure B.2: Single slit isothermal analysis ; $\phi_g = 3.2$.

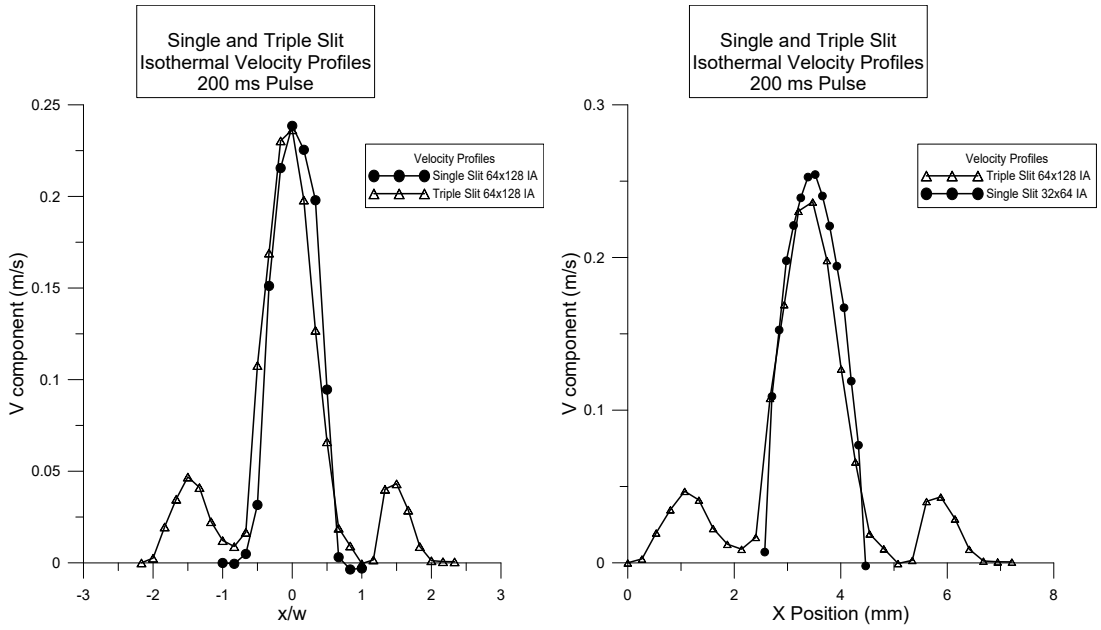

(a) Single slit velocity measurements ; $\phi_g = 3.2$.

(b) Triple and single slit velocity measurements ; $\phi_g = 3.2$.

Figure B.3: Single and triple slit isothermal analysis ; $\phi_g = 3.2$.